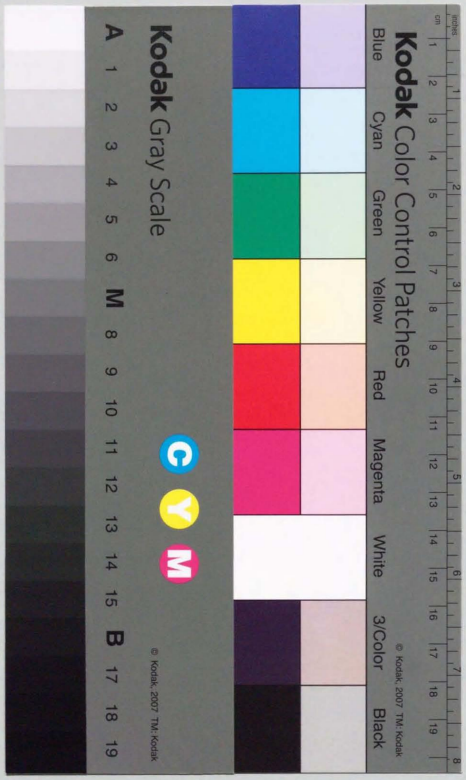

学位論文

Theoretical Models for Type Ia Supernovae
and the Hubble constant

Ia 型超新星の理論的モデルと ハッブル定数

平成 4 年 12 月博士 (理学) 申請

山 岡 均

Theoretical Models for Type Ia Supernovae and the Hubble constant

Hitoshi YAMAOKA

December 1992

Abstract

The determination of the Hubble constant by measuring the distance to the distant galaxies with their recession velocities is fundamental to cosmology. The method using type Ia supernovae as standard candles is promising on the observational basis, but their absolute brightness has not been determined precisely.

We present in this paper several models for type Ia supernovae, for which the theoretical light curves are calculated and their maximum absolute luminosities are obtained. With these supernovae models, we estimate the plausible the Hubble constant.

To account for some varieties of type Ia supernovae, we introduce a *late detonation model* into the standard carbon deflagration model. In this model, a carbon deflagration, producing a central Fe/Co/Ni core and an intermediate Si/S/Ca layer, is later transformed into a detonation in the outermost layer. Depending on the transition density, the synthesized elements ratio in the detonation region changes, which explains the inferred composition of recently observed supernovae 1991T and 1990N qualitatively in a unified manner.

The light curves for late detonation models as well as carbon deflagration models are calculated. These light curves with somewhat larger optical opacities than in earlier works are in good agreement with the corresponding supernovae observation, whose premaximum rise time is as large as 20 days with broader peak. To distinguish deflagration models from late detonation models, line γ-ray observation in early phase is crucial.

We have estimated the Hubble constant by comparing the theoretical light curve with the observed light curve of type Ia supernovae. Our estimate is $H_0 = 73 \pm 10$, which is somewhat larger than that previously estimated from type Ia supernovae.

Contents

Chapter 1

Introduction

1.1 Distance measurement

The Hubble's law is fundamental to the Big Bang cosmology. However, the Hubble constant H_0 has not been determined to a good accuracy, ranging from 40 to 100 km s^{-1} Mpc^{-1}. This is mainly caused by the difficulty in the determination of the distances to galaxies. On the other hand, the radial velocity can be determined accurately by the spectroscopic observations.

The measurement of the distances to stars and galaxies have long been carried out. The distances of very nearby stars, including planets, can be measured by triangular surveying using the diameter of the Earth and the Earth's orbit as the baseline. This method is, however, available only for the stars locating within 100 pc. For more distant targets, we have to use other methods. The main method for distance determination is the usage of objects with known absolute magnitudes, namely 'Standard Candles'.

The most well-known standard candles are Cepheids, whose absolute magnitudes are estimated from their pulsating periods. Their absolute magnitudes, $\sim -6^m$ for the brightest one, are not sufficient to be found out in distant galaxies. The most distant Cepheid ever found locates in IC 4182, reported by A. Sandage using Hubble Space Telescope (Crosswell 1992 [15], Schwartzschild 1992 [68], Sandage *et al.* 1992 [66]). The distance to IC 4182 is only about 5 Mpc, so that we can not measure even the distance to the nearest cluster of galaxies, the Virgo cluster, with this method.

Using galaxies themselves as standard candles is being attempted. The most famous relation which connects the observation to the absolute luminosities of galaxies would be

the Tully-Fisher relation, which shows that the rotation velocity of a spiral galaxy has a good correlation to its absolute magnitude. This rotational velocity is measured from the line width, so that the distances to the galaxies which locate nearer than ~100 Mpc can be estimated with the Tully-Fisher method. However, this relationship is only empirical with no theoretical basis. In the course of getting the 'zero point' of this relationship, the distance ladder method can not be avoided. Each step of this ladder would have some error, so that the total error would become somewhat large.

In order to determine the Hubble constant, we have to observe galaxies further than several tens of Mpc to reduce the contribution from the peculiar motions of galaxies and the systematic motions of galaxies (e.g. Virgo infall) in the measurement of the recession velocities. If we can use another standard candle whose absolute luminosity is known and as bright as a galaxy, the distance measurement of some hundreds Mpc would become more reliable. Thus, a supernova(SN), which is as bright as a whole galaxy in their peak luminosity, is expected to be used in the distance measurement.

1.2 Type Ia supernovae as standard candles

Supernovae(SNe) are classified from their spectra and light curves. Among them, type Ia supernovae (SNe Ia) are characterized by the absence of Hα absorption and the existence of deep and broad Si II absorption lines in their maximum light. SNe Ia are the brightest among supernovae, thus being found in more distant galaxies than other types of supernovae.

The observations of SNe Ia have revealed that SNe Ia have light curves with the similar shapes and homogeneous spectral evolutions. It is in contrast to type II supernovae (which are categorized with deep Hα absorption), whose light curves or spectra differ from one another. Then, it should be expected that SNe Ia are similar in their peak absolute luminosities as well as in the shapes of their light curves. If so, we can use them as standard candles.

Recently, the uniformity in their peak luminosities has been discussed observationally. There are some methods to confirm this:

1) SNe Ia occurred in the Virgo cluster.

Some investigators have dealt SNe Ia in the Virgo cluster, which is the nearest cluster of galaxies (Capaccioli *et al.* 1990 [12], Branch, Tammann 1992, hereafter BT92 [8]). There are 6 supernovae of this type whose peak B magnitudes were well observed and which are confirmed to belong to the members of the Virgo cluster. If these supernovae are able to be regarded as at the same distance, they should have the same peak brightness. The dispersion of $m_{\mathrm{B,max}}$ is 0.36, and after the correction of parent-galaxy extinction which is estimated from B-V observation, this value decreases to 0.27. This dispersion would be well explained by errors of distances, Galactic extinction, apparent magnitude derivation (BT92 [8]).

2) Two SNe Ia in the same galaxy.

There are some galaxies in each of which two SNe Ia have been observed. BT92 [8] treated three pairs of SNe Ia, and concluded that there is a very small dispersion in the B maximum ($\Delta m_{\mathrm{B}} = 0.11$) after correction of the extinction by host galaxies (see Sec. A.1).

3) Plot on the Hubble diagram.

If SNe Ia have the same peak absolute luminosities, the Hubble diagram of them, i.e., the plot of logarithm of radial velocities of their host galaxies versus peak apparent magnitudes of supernovae, will line up in a straight line for the region of $z \ll 1$. Tammann, Leibundgut (1990) [74] made this diagram using 35 SNe Ia which emerged in some distant galaxies with large recession velocities in order to avoid the influence of peculiar motions of their host galaxies. The mean dispersion in the observed peak magnitudes from the Hubble line is $\sigma_{\mathrm{B}} = 0.57$, and after being corrected by some assumed peculiar motions, it decreases to 0.25.

All of these made the same conclusion that the peak absolute luminosities of SNe Ia are not so dispersed and we can use them as standard candles. But, before using them as standard candles, we have to estimate the peak absolute luminosities for determining the 'zero point'. Several ways for observational estimation of this value are considered:

a) historical Galactic supernovae:

Among the historical Galactic supernovae, SN 185, SN 1006, SN 1572 (Tycho's star), and SN 1604 (Kepler's star) are considered to be of type Ia. The distances to their remnants are measured by Strom (1988) [72]. Connecting them with the estimation of apparent peak magnitudes from (not so precisely quantitative) records (Clark, Stephenson 1977 [13], 1982 [14]), and estimating the Galactic extinction by some methods, BT92 [8] shows that the peak $M_B \sim -20$. But they attach importance only to Kepler's star, because Tycho's star might be of type Ib and both of SN 185 and SN 1006 were not seen by scientific eyes. The absolute visual magnitude of Kepler's star is estimated to be -19.7 ± 0.6 after correction of the extinction.

b) nearby SNe Ia:

There is only one galaxy in which a SN Ia has been observed and on the other hand whose distance has been estimated by using Cepheid. The group organized by Sandage found out 27 Cepheids in IC 4182 using Hubble Space Telescope, and estimated that this galaxy lies 16 million light years away (Sandage *et al.* 1992 [66]). The peak magnitude of SN Ia 1937C in IC 4182 was $m_{pg} = 8.50$ and $m_V = 8.55$ (Leibundgut *et al.* 1991; hereafter LTCC91 [41]), and assuming that $A_V = 0.0$ for Galactic extinction after LTCC91 [41], M_V is estimated as -19.92 ± 0.13.

For other nearby galaxies with observed SNe Ia, their distances are measured by other methods such as planetary nebula method (van den Bergh 1989 [79]). For example, SN 1972E in NGC 5253 is estimated that $M_B \sim -19.7$ (BT92 [8]).

c) SNe Ia in the Virgo cluster:

For 6 SNe Ia in the Virgo cluster, the mean apparent blue magnitude is estimated as $m_B = 11.91 \pm 0.18$ (Leibundgut, Tammann 1990 [40]). But there exists a difficult problem in the determination of the distance to the Virgo center. There exists large dispersion in the distance to the Virgo depending on the methods. If we take 20.0 ± 3.0 Mpc as this value, same as BT92 [8], $M_B = -19.60 \pm 0.51$.

All of these method have a difficulty in the determination of the distance. This is the

same situation as using Tully-Fisher relation or so; the ambiguity in using the distance ladder. To avoid this difficulty, we should estimate the peak absolute luminosity of type Ia supernovae in the other method, say, *theoretically*. This is the motivation of this paper.

1.3 Theoretical models for SNe Ia

For the origin of SNe Ia, accreting white dwarfs have been considered to be promising candidates of their progenitors. The explosion mechanism originally suggested by Hoyle, Fowler (1960) [27], i.e., the thermonuclear explosion of electron-degenerate cores, basically has been confirmed by extensive numerical modeling and comparison with observations (Nomoto 1986 [49]; Woosley, Weaver 1986b [86]).

Isolated white dwarfs are simply cooling stars that eventually end up as invisible frigid stars. The white dwarf in a close binary system evolves differently because the companion star expands and transfers matter over to the white dwarf at a certain stage of its evolution. The mass accretion can *rejuvenate* the cold white dwarf (e.g., Nomoto, Sugimoto 1977 [57]), which could lead to a type Ia supernova.

The scenario that possibly brings a close binary system to a SN Ia is as follows (although the exact evolutionary origin has not been understood): Initially the close binary system consists of two intermediate mass stars ($M \lesssim 8\ M_\odot$). As a result of Roche lobe overflow, the primary star of this system becomes a white dwarf composed of carbon and oxygen (C+O). When the secondary star evolves, it begins to transfer hydrogen-rich matter over to the white dwarf.

The mass accretion onto the white dwarf releases gravitational energy at the white dwarf surface. Most of the released energy is radiated away from the shocked region as UV and does not contribute much to heating the white dwarf interior. The continuing accretion compresses the previously accreted matter and releases gravitational energy in the interior. A part of this energy is transported to the surface and radiated away from the surface (*radiative cooling*) but the rest goes into thermal energy of the interior matter (*compressional heating*). Thus the interior temperature of the white dwarf is determined by the competition between compressional heating and radiative cooling; i.e., the white dwarf is hotter if the mass accretion rate $\dot{M}$ is larger, and vice versa (e.g., Nomoto,

Hashimoto 1987 [52]).

When carbon is ignited at the center of the white dwarf whose mass is close to the Chandrasekhar mass, carbon burning is so explosive as to incinerate the material into iron-peak elements; the central temperature reaches $\sim 10^{10}$ K. At such a high central density as $\gtrsim 10^9$ g cm^{-3}, nuclear energy release is only ~ 20 % of the Fermi energy of degenerate electrons. Therefore, the resulting shock wave is not strong enough to directly ignite carbon in the adjacent layer. In other words, a *detonation* wave that propagates at supersonic speed does not form.

Instead, the interface between the burned and unburned layers becomes convectively unstable. As a result of mixing with the hot material, fresh carbon is ignited. In this way, a carbon burning front propagates outward on the time scale for convective heat transport (Nomoto, Sugimoto, Neo 1976 [58], Nomoto, Thielemann, Yokoi 1984, hereafter NTY [59]; Woosley, Weaver 1986a [85], b [86]). This kind of explosive burning front that propagates at a subsonic speed is called a *convective deflagration* wave. In the model W7 (NTY [59]), the propagation speed of the convective deflagration wave is on the average about one-fifth of the sound speed. It takes about one second for the front to reach the surface region, which is significantly slower than the supersonic detonation wave. Hence the white dwarf expands during the propagation of the deflagration wave.

Behind the deflagration wave, the material undergoes explosive burning of silicon, oxygen, neon, and carbon depending on the peak temperatures. In the inner layer, nuclear reactions are rapid enough to incinerate the material into iron-peak elements, mostly ^{56}Ni. When the deflagration wave arrives at the outer layers, the density it encounters has already decreased due to the expansion of the white dwarf. At such low densities, the peak temperature is too low to complete silicon burning and thus only Ca, Ar, S, and Si are produced from oxygen burning. In the intermediate layers, explosive burning of carbon and neon synthesizes S, Si, and Mg. In the outermost layers, the deflagration wave dies and C+O remain unburned. The composition structure after freeze-out is shown as a function of M_r and the expansion velocity in Figure 1.1.

In the carbon deflagration model W7, the amount of ^{56}Ni produced is $M_{\rm Ni} = 0.58\ M_\odot$, and the explosion energy is E = (Nuclear energy release – Binding energy of the white

dwarf) $= 1.3 \times 10^{51}$ erg. The nuclear energy release is large enough to disrupt the white dwarf completely and no compact star is left behind.

Because SNe Ia do not have a thick hydrogen-rich envelope, elements newly synthesized during the explosion can be observed in the spectra; this enables us to diagnose the internal hydrodynamics and nucleosynthesis in SNe Ia.

Synthetic spectra are calculated based on the abundance distribution and expansion velocities of the carbon deflagration model W7 and are found to be in excellent agreement with the observed optical spectra of SN 1981B (Branch *et al.* 1985 [7]) and 1989B (Figure 1.2; Harkness 1991a [23]). In Figure 1.2, the calculated spectrum for the stratified composition is in better agreement than for the mixed composition. The material velocity at the photosphere near maximum light is $\sim 10{,}000$ km s^{-1} and the spectral features are identified as P-Cygni profiles of Fe, Ca, S, Si, Mg, O.

At late times, the spectra are dominated by the emission lines of Fe and Co. The outer layers are transparent and the inner Ni-Co-Fe core is exposed. Synthetic spectra of emission lines of [Fe II] and [Co I] for the carbon deflagration model agree quite well with the spectra observed at such phase (Axelrod 1980 [3]; Woosley, Weaver 1986b [86]).

The good agreement between the calculated and observed spectra (especially near maximum light) implies that the composition structure as a function of velocity for SNe Ia must be similar to W7 in spite of serious remaining uncertainties associated with the presupernova evolution of the binary systems, the initiation of deflagration rather than detonation, and the propagation of the burning front.

1.4 New observational features of SNe Ia

1.4.1 Rise time to maximum light

It had been believed that the rise time t_R of SNe Ia, i.e., the time from the explosion to light maximum, would be relatively short, because there are little examples of SNe Ia which were discovered one week before well-defined light maximum (for examples, see LTCC91 [41]). Cadonau, Sandage, Tammann (1985) [10] derived that t_R is less than 20 days from the composed blue light curve.

Recently, some of SNe Ia were discovered well before light maximum. SN 1990N in

NGC 4639 was discovered on 1990 June 22.96 UT [46] and the epoch of its maximum of B magnitude was estimated on July 10.5 ± 1.0 (Leibundgut *et al.* 1991 [39]). The value of t_R is obviously larger than 17 days for SN 1990N, and is estimated as 20 days or so (see Figure 1.3). SN 1991T in NGC 4527 is also discovered well before maximum. The earliest detection was made by S. Knight on 1991 April 13.17 UT visually (Waagan *et al.* 1991 [82]). The plate obtained at Palomar Observatory on April 10.26 – 10.32 UT showed no object at the point of SN 1991T with the limiting near-infrared magnitude of 19.5 [82]. Visual maximum of SN 1991T occurred on April 27 ± 1, then t_R is estimated as 16 ± 2 days (Filippenko *et al.* 1992a [19]). On the ground of these observation, Branch (1992) [6] estimates that the mean t_R is 19 ± 2 days.

1.4.2 Variations of SNe Ia

Recent observations of SNe Ia before maximum brightness, providing new information on the composition of the outermost layers of SNe Ia, challenge the current theoretical models (see e.g., Nomoto *et al.* 1992 [60] for a review):

(i) The pre-maximum spectra of SN 1990N (Leibundgut *et al.* 1991 [39]) indicate the presence of Si, Ca, Fe, and Co in the outermost layers with $v_{exp} \sim 20{,}000$ km s^{-1}.

(ii) SN 1991T has shown quite a unique spectral evolution: the pre-maximum spectrum is dominated by Fe/Ni lines, while the spectra after maximum light show typical SNe Ia features, characterized first by Si/S/Ca lines, and becoming later Fe-dominated (Filippenko *et al.* 1992a [19] ; Ruiz-Lapuente *et al.* 1992 [65]). The inferred composition structure of SN 1991T is as follows:

(I) The outermost layer is composed of Ni and Fe with expansion velocities $v_{exp} \sim 13{,}000$ km s^{-1}.

(II) The intermediate layer is rich in Si/Ca with $v_{exp} \sim 10{,}000$ km s^{-1}.

(III) The central layer is again dominated by Fe (Filippenko *et al.* 1992a [19]).

In other words, the Si/S/Ca-rich layer (II) is sandwiched by the two Fe layers (I and III). Such a composition *inversion* with Fe above Si is very different from that inferred

from SNe Ia ever observed. On the other hand, the composition of the inner layers (II and III) is very similar to those of typical SNe Ia including SN 1990N (Filippenko *et al.* 1992a [19]; Phillips *et al.* 1992 [63]).

The composition of the inner layers (II) and (III) (i.e., the intermediate Si/Ca layer and the central Fe layer) of the above SNe Ia may be accounted for by the carbon deflagration model W7 (NTY [59]). However, the presence of high velocity heavy elements in these SNe Ia is not consistent with W7, because the highest velocities of newly synthesized elements in W7 are $\sim$ 15,000 km s^{-1} (see Figure 1.1) and the outermost layer is dominated by O and C.

Modeling of these new pre-maximum features is urged, since it can provide a new clue to the long debated problems of the progenitors of SNe Ia, the explosion mechanism, and the uniformity of SNe Ia. Especially, it is important to clarify whether SN 1991T belongs to a different subclass of SNe I (e.g., SNe Id; Branch, Tammann 1992 [8]) or is only a small variant of SNe Ia. From these studies, we can estimate the intrinsic dispersion of SNe Ia from theoretical side.

In Chapter 2, the models of SNe Ia are discussed. To account for the observed spectroscopic and photometric features of SNe Ia 1990N and 1991T, we introduce a late detonation model into the standard carbon deflagration model. The late detonation model assumes that the central carbon deflagration is transformed into detonation near the surface in some case of thermonuclear explosions. In Chapter 3 we present the theoretical light curves of the late detonation models as well as the carbon deflagration model with an improved energy deposition function obtained from the Monte Carlo simulation. In Chapter 4 we have estimated the Hubble constant by comparing the theoretical light curve with the observed light curve of SNe Ia. Chapter 5 is the conclusion.

Chapter 2

Theoretical Models for Type Ia Supernovae — Carbon Deflagration and Late Detonation

2.1 Possible models for SNe 1990N and 1991T

There are four possible models for the premaximum features of SN 1990N. Among them,

(i) mixing adds Si, Ca, and Fe to the outer layers of W7 (Branch *et al.* 1985 [7]; Branch, Venkatakrishna 1986 [9]); it may, however, be difficult to cause a composition inversion with Fe/Ni in the outermost layers as in SN 1991T.

(ii) The delayed detonation models assume that an initially very slow deflagration turns into a detonation relatively deep in the interior (Khokhlov 1991b [32]; Woosley, Weaver 1992 [87]); such an event produces high velocity Si/Ca, but it is difficult to synthesize Fe again near the surface.

(iii) The carbon detonation models for low mass white dwarfs (Shigeyama *et al.* 1992 [71]) have the same difficulty in explaining SN 1991T.

If one of the cases (i)–(iii) is the actual model for SN 1990N, then it is likely that SN 1991T resulted from a somewhat different explosion mechanism, thus belonging to a different subclass of SNe I (e.g., SNe Id).

The remaining possibility;

(iv) As given in Shigeyama *et al.* (1992) [71], the formation of a detonation in the outermost layers, induced by a fast propagation of a deflagration wave.

NTY [59] noted that the carbon deflagration model C8, whose propagation velocity $v_{\rm def}$ is slightly higher than W7, has a precursor shock which is strong enough to induce a detonation in the outer layers (see also Woosley, Weaver 1986a [85]). In view of the small difference in $v_{\rm def}$ between W7 and C8, the deflagration in W7 can be regarded as marginal in forming a detonation in the outer layers.

The transition from a deflagration to a detonation can occur when the propagation velocity of the deflagration wave $v_{\rm def}$ is accelerated to the Chapman-Jouguet velocity $v_{\rm CJ}$. The transition is more likely to occur at lower densities, because the ratio $v_{\rm CJ}/v_{\rm s}$ ($v_{\rm s}$ denotes the sound velocity) is smaller due to a larger density jump across the burning front (Khokhlov 1991a [31]), while $v_{\rm def}/v_{\rm s}$ is larger (NTY [59]). Since the convective deflagration front may well be quite turbulent and the acceleration of $v_{\rm def}$ may take place in an indeterministic manner, the condition of the transition from deflagration to detonation has not been well understood (e.g., Williams 1985 [83]) and it could occur even for $v_{\rm def} < v_{\rm CJ}$. It is also possible that a relatively small difference in $v_{\rm def}$ in the deeper layers could cause a large variation in the transition density in the outer layers. Such a difference in $v_{\rm def}$ may stem from differences in ignition conditions, such as the central density (i.e. the age and the accretion rate) of the white dwarf.

It should be mentioned that before a multidimensional high resolution calculation of such burning fronts is undertaken, which is extremely difficult if not impossible at present, $v_{\rm def}$ is an unknown parameter. It can therefore not be decided, whether initially slow deflagrations (Khokhlov 1991b [32]) or W7-type fast deflagrations (NTY [59]) are adequate. In the light of recent modeling of synthetic spectra for generic SNe Ia (Harkness 1991a [23]) and also 1990N and 1991T (Jeffery *et al.* 1992 [30]), which all come to the conclusion that the spectra are consistent with W7-like central cores of SNe Ia, we chose to explore variations along this line.

In this chapter, we present several hydrodynamical models for case (iv); here the carbon deflagration, producing a central Fe/Co/Ni core and an intermediate Si/S/Ca layer, is later transformed into a detonation in the outermost layers, which we call a *late detonation*. We show that nucleosynthesis in the detonated matter depends sensitively on the density at the transition from deflagration to detonation. We suggest that a variation

of nucleosynthesis (e.g., ^{56}Ni/Si ratio) in such late detonations may possibly account for both SN 1990N and SN 1991T in a unified manner, i.e., SN 1991T may well be a small variant of SNe Ia.

2.2 Deflagration models and late detonation models

To construct the models of SNe Ia, we start from the C+O white dwarf that accretes matter at a rate of $4 \times 10^{-8}\ M_\odot\ \mathrm{yr}^{-1}$ up to a mass of 1.378 $M_\odot$ and eventually ignites carbon at the center with $\rho_c \sim 3 \times 10^9\ \mathrm{g\ cm}^{-3}$ (NTY [59]). Afterwards the white dwarf is assumed to undergo carbon deflagration until the transition to a late detonation takes place in the outer layers. The adopted carbon deflagration models are W7 and W8 (NTY [59]), where the ratio between the mixing length and a scale height of pressure for convective deflagration is $\ell/H_p = 0.7$ (W7) and 0.8 (W8). Thus the propagation speed of the deflagration is faster in W8 than in W7 by a factor of ~ 1.2.

Since W8 is very similar to C8 (NTY [59]), except for the presupernova accretion rate, and the difference in v_{def} between W7 and W8 is not large, both W7 and W8 may be marginal in inducing a late detonation.

In the present study, we mainly investigate the late detonation in W7. First, some late detonation models whose transition point from deflagration to detonation differ are figured. After that, we attention with detailed nucleosynthesis to two cases of the late detonation in W7 with the transition at $M_r = 1.12\ M_\odot$ (W7DT) and 1.20 $M_\odot$ (W7DN), respectively. These cases assume that a small difference in v_{def} in the inner layer leads to a significant difference in the transition point. In addition, the transition from the deflagration W8 to a late detonation at $M_r = 1.25\ M_\odot$ (W8DT) is simulated for comparison.

As an alternative case, we also study the case that the initial white dwarf has a thick helium layer at $M_r > 1.20\ M_\odot$ and the transition from W7 to late detonation occurs at the bottom of the helium layer (W7DHE). Note that this configuration is rather artificial as discussed in 2.4.3.

The detonation wave is initiated by artificially accelerating v_{def} (Shigeyama *et al.* 1992 [71]). The initial composition in the unburned outer layers is set that the mass fractions of ^{12}C, ^{16}O, and ^{22}Ne are 0.48, 0.50, and 0.02 with a neutron excess of 0.002

($Y_e = 0.499$). The numerical calculation is performed with a 1D Lagrangian PPM code coupled with an energy generation network including 13 nuclear species (see Shigeyama *et al.* 1992 [71]). The detailed nucleosynthesis for models W7DN, W7DT, W7DHE, and W8DT is calculated with a larger nuclear reaction network of 299 species (Thielemann, Nomoto, Yokoi 1986 [77] ; Thielemann, Hashimoto, Nomoto 1990 [75]). The remaining input physics is basically the same as adopted in Nomoto, Kondo (1991) [54].

2.3 Dependence on the transition point

The early evolution of late detonation models based on W7 is the same as W7 (see NTY [59]), i.e., a carbon deflagration wave forms at the center and propagates outward until the late detonation is initiated. Nucleosynthesis in the deflagration phase is sensitive to the peak temperature T_p which decreases as the deflagration wave propagates outward because of the expansion of the white dwarf. About W7, in the interior to $M_r \sim 0.78 M_\odot$, the matter undergoes complete silicon burning to iron peak elements. In the region $\lesssim 1.02\ M_\odot$, incomplete silicon burning produces ^{56}Ni, Ca, Ar, S, and Si. At $1.02\ M_\odot \lesssim M_r \lesssim 1.28\ M_\odot$, explosive burning of oxygen and carbon produces Si and Ca. (See Figure 1.1.)

At an assumed location, the deflagration wave is transformed into a detonation wave, which quickly develops to propagate self-consistently at the speed of a Chapman-Jouguet detonation. Behind the detonation wave, material undergoes explosive nuclear burning. Its products are sensitive to T_p, which in turn depends on the density at the burning front. For the same initial density, the detonation wave has a higher density than the deflagration because of the shock compression, thereby attaining a higher T_p. Accordingly, the detonation wave in the outer layers produces heavier elements than those produced by the deflagration in the inner layers, if this transition occurs in the intermediate elements zone. In other words, a composition inversion is naturally formed.

For the survey, the transition points are set on at $M_r = 0.82\ M_\odot$, 0.94 $M_\odot$, 1.00 $M_\odot$, 1.08 $M_\odot$, 1.18 $M_\odot$, 1.20 $M_\odot$, and 1.24 $M_\odot$. The mass of iron peak elements and the mass of Si are shown in Table 2.1, which are produced in deflagration region (inner than the transition) or late detonation region (outer), separately. The expansion velocities at the

transition point, i.e., maximum v_{exp} of inner Si, are also presented in Table 2.1.

Basic characteristics of those models are as follows: as the transition point moves outer,

a) The mass of iron peak elements in late detonation region decreases.

b) The mass of Si in late detonation region increases except for the last model.

c) The mass of iron peak elements in deflagration region is basically the same, but slightly decreases. The first model is an exception.

d) The mass of Si in deflagration region increases.

e) In the last model, late detonation does not occur.

These characteristics can be understood easily. The outer the transition point moves, the lower the density becomes there, and then the less explosive the nucleosynthesis by late detonation becomes. For the first model, the transition occurs in the region of incomplete silicon burning, so the mass of iron peak elements produced in deflagration region is smaller than other models because of the cut off at the transition point. And the amount of Si produced in deflagration region changes due to the movement of the transition (cut off) point.

If the transition occurs in the region of incomplete silicon burning, the amount of Si in the inner is so small that Si II absorption line at the maximum light would not be able to be observed. So, for a real model of SNe Ia, we should refuse the late detonation models whose transition occur inner than 1.0 $M_\odot$. Now, we focus the models whose transition points are in outer, so we treat W7DT or W7DN with the detailed nucleosynthesis code in the next section.

2.4 Nucleosynthesis

About real nucleosynthesis in SNe Ia, in the very central region, neutronization due to electron capture leads to the production of ^{56}Fe, ^{57}Fe, and ^{57}Ni. Then, ^{56}Ni in this region is very small, and the total amount of this species is smaller than calculated in previous section which is mentioned as iron peak elements.

As mentioned above, we calculate 4 late detonation models with a detailed nuclear reaction network. The main characteristics of those models, such as the mass of produced ^{56}Ni or M_r of the transition points, are summarized in Table 2.2. Detailed composition structure of W7 and late detonation models are presented in Tables 2.3 $\sim$ 2.7.

2.4.1 Model W7DN

In this model, the transition from deflagration to detonation is set to occur at $M_r = 1.20$ $M_\odot$. At this stage, $T_p \sim 3 \times 10^9$ K behind the deflagration wave and explosive carbon burning is forming O-Ne-Mg layers. The density ahead of the burning front is $\rho_0 = 1.7 \times 10^7$ g cm^{-3}. After the late detonation is started, T_p gets as high as 5×10^9 K. This temperature leads to incomplete silicon burning which synthesizes some ^{56}Ni and Si/Ca. At 1.21 $M_\odot < M_r < 1.28$ $M_\odot$, the mass fraction of ^{56}Ni is $\sim 0.5 - 0.3$ and the rest is Si and Ca.

As the detonation wave propagates to the lower density layers, T_p decreases and explosive burning of oxygen, neon, and carbon takes place accordingly. The resultant composition structure of W7DN is shown in Figure 2.1 as a function of v_{exp} and M_r. Here v_{exp} denotes the homologous expansion velocity which is attained in 10 sec after the initiation of the deflagration. The production of ^{56}Ni by incomplete silicon burning extends from $v_{exp} \sim 14{,}000$ km s^{-1} to 30,000 km s^{-1}, and Ca, Ar, S, and Si are produced from explosive burning of oxygen, neon, and carbon up to $v_{exp} = 35{,}000$ km s^{-1} (Ca) and 50,000 km s^{-1} (Si). The mass of ^{56}Ni is $M_{Ni} = 0.63$ $M_\odot$ and the explosion energy is $E = 1.4 \times 10^{51}$ erg.

2.4.2 Models W7DT and W8DT

These models undergo the transition from deflagration to detonation at a higher density than W7DN, i.e., $\rho_0 \sim 3.5 \times 10^7$ g cm^{-3} ahead of the deflagration wave. This corresponds to the transition at $M_r = 1.07$ $M_\odot$ (W7DT) and 1.25 $M_\odot$ (W8DT) because of the difference in v_{def} between W7 and W8.

At the transition to the detonation, the peak temperature T_p increases from 4×10^9 K to 5.5×10^9 K, which is significantly higher than in W7DN. Therefore, the material at 1.07 - 1.17 $M_\odot$ in W7DT (1.25 - 1.32 $M_\odot$ in W8DT) undergoes almost complete silicon

burning, producing mostly ^{56}Ni with a mass fraction as large as 0.9.

As the detonation wave propagates outward, incomplete silicon burning takes place. The ^{56}Ni abundance decreases because of the lower T_p. The mass fractions of Ca and Si are still smaller than $\sim 0.03 - 0.05$ at $M_r < 1.23\ M_\odot$ for W7DT ($M_r < 1.33\ M_\odot$ for W8DT) and the outer layers are rich in Si and Ca with small amounts of ^{56}Ni.

The composition structure of W7DT (W8DT) as a function of M_r and v_{exp} is shown in Figure 2.2 (Figure 2.3). In velocity space, ^{56}Ni in the detonated layers extends from $\sim$ 12,000 km s^{-1} to 30,000 km s^{-1} for W7DT (from 15,000 km s^{-1} to 50,000 km s^{-1} for W8DT). Intermediate mass elements are produced up to $v_{exp} \sim$ 40,000 km s^{-1} (W7DT) and 50,000 km s^{-1} (W8DT) for Ca, and $\sim$ 50,000 km s^{-1} (W7DT) and 60,000 km s^{-1} (W8DT) for Si. The explosion energy is 1.5×10^{51} erg for both cases, and the ^{56}Ni masses are 0.78 $M_\odot$ (W7DT) and 0.80 $M_\odot$ (W8DT).

Figure 2.2 clearly reveals a composition inversion with an Fe dominated layer above the Si-rich layer. Note that such an apparent composition inversion is not formed if the transition occurs when the deflagration is still incinerating the material into iron peak elements as in the case of delayed detonation models (Khokhlov 1991b [32]; Woosley, Weaver 1992 [87]).

2.4.3 Model W7DHE

This model undergoes the transition from deflagration to detonation at $M_r = 1.20\ M_\odot$ as in W7DN. Because of the presence of helium at $M_r > 1.2\ M_\odot$, the deflagration is naturally transformed into a helium detonation (i.e., without artificial acceleration of v_{def}).

Due to the larger energy release in the helium detonation, the peak temperature reaches $T_p \sim 6 \times 10^9$ K, being significantly higher than in W7DN. Such a high T_p has two effects:

(1) The detonated material is processed into a ^{56}Ni-dominated composition, where $\sim$ 10 percent helium by mass remains due to an α-rich freeze out. Almost no Si/Ca is produced. In the outermost layers at $M_r > 1.35\ M_\odot$ and $v_{exp} >$ 30,000 km s^{-1}, the mass fraction of helium exceeds 0.2 and trace intermediate mass elements appear.

(2) The helium detonation sends an inward shock wave, which burns O+Ne+Mg into Si-rich material.

The resulting abundance distribution is shown in Figure 2.4. Since the helium detonation has a stronger shock front than the carbon detonation in W7DT, $E = 1.7 \times 10^{51}$ erg and $M_{Ni} = 0.73\ M_\odot$.

2.4.4 Effects of metallicity

We would like to defuse an argument often used against W7: the non-solar composition of Fe-group isotopes, especially for ^{54}Fe and ^{58}Ni, while SNe Ia are the main contributors (Woosley, Weaver 1992 [87]). These two isotopes originate from mass zones with intermediate neutron excess, which can be either caused by electron capture in the core or initial metallicity of the white dwarf in the outer layers where CNO nuclei were transformed to ^{22}Ne after H and He burning. As most SNe Ia occur in spiral galaxies on scale heights larger than 300 pc (Della Valle, Panagia 1992 [16]) where [Fe/H] values are 0.0 to $-$ 0.5 (Fig. 11.5 in Gilmore 1989 [21]), one has *average* metallicities of 0.5–0.6 times solar. We have recalculated W7 with zero metallicity and find the ^{54}Fe/^{56}Fe and ^{58}Ni/^{56}Fe ratios within a factor of 2 and 3 of solar, respectively (Thielemann *et al.* 1992 [76]). This lies within the present uncertainty range of thermonuclear reaction rates and is therefore consistent with a solar composition. A factor of 1/2 in neutron excess is already sufficient to make the amounts of ^{54}Fe and ^{58}Ni in the outer layers negligible in comparison to the inner core and gives essentially the same results as for zero neutron excess (metallicity).

2.5 Comparison with SN 1990N and SN 1991T

As summarized in section 1.4.2, the similarity in the near and post-maximum spectra from SN 1991T and SN 1990N to those from typical SNe Ia suggests that the composition distribution in velocity space for the inner Si/Ca layers (II) and the Fe-rich core (III) is similar to that of SNe Ia. Since the spectra in these phases are well accounted for with the carbon deflagration model W7 (Harkness 1991a [23]; Jeffery *et al.* 1992 [30]), the inner structure of W7DN, W7DT and W7DHE is expected to be consistent with SNe 1990N and 1991T. Then the question is whether the composition in the outermost layers (I) of these supernovae can be accounted for by these late detonation models.

Among the models presented in 2.4, W7DN has a significant amount of Si, Ca, and ^{56}Ni at expansion velocities as high as $v_{\rm exp} \gtrsim 20{,}000$ km s^{-1}. The other three models (W7DT, W8DT, and W7DHE) have a Si/Ca layer being sandwiched by the Ni/Fe dominant layers. Therefore, the basic features of the Si and Fe distributions in W7DN and W7DT/W8DT/W7DHE are qualitatively in agreement with the spectroscopic features of SN 1990N and SN 1991T, respectively.

For detailed comparison with observations, the following abundance features of layer (I) should be noted:

(i) The outermost Ni-rich layer of W7DT and W8DT contains some high velocity Si and Ca. Since W8DT undergoes the transition to detonation at larger M_r than W7DT, it contains smaller amounts of Si and Ca.

(ii) In contrast, the layer (I) of W7DHE contains only trace abundances of Si and Ca but a significant amount of He.

(iii) These three models contain rather little O and Mg.

Whether the amounts of Si/Ca, He, and O/Mg are consistent with the pre-maximum spectra of SN 1991T should be examined with detailed synthetic spectra (Jeffery *et al.* 1992 [30]). Because of the presence of radioactive ^{56}Ni in the outermost layers, the spectra would be highly NLTE. Whether the helium features excited by γ-rays (Lucy 1991 [45]) appear or not would be a crucial diagnosis of not only W7DHE but also a possible alternative model of off-center helium detonation (Filippenko *et al.* 1992a [19]; Livne 1990 [44]; Nomoto 1982b [48]). An examination of the synthetic spectra for the present models is underway in collaboration with D. Jeffery.

With regard to O and Mg, it seems more likely that the transition to a detonation occurs at several points rather than in a spherical shell. The resulting carbon detonation may leave some unburned or partially burned C, O, Ne and Mg. This possibility is currently being examined with 2D and 3D hydrodynamical simulations. Another possibly important process is the deceleration of the ejecta by circumstellar matter, which would induce some mixing between the outermost Ni layer and the circumstellar matter.

From the evolutionary point of view, the assumed presence of a thick helium layer in W7DHE might be realized if the accretion of helium takes place so slowly that helium

is too cold to be ignited (Nomoto 1982a [47],b [48]). Note, however, that such a slow accumulation of helium may occur only through nova explosions, thereby being extremely difficult if not impossible. Also the central region of the white dwarf with such a slow accretion must be solid when carbon is ignited at $\rho_{\rm c} \sim 10^{10}$ g cm^{-3}; therefore, a collapse is more likely to occur rather than an explosion (Nomoto 1987 [50]; Nomoto, Kondo 1991 [54]; Canal *et al.* 1990 [11]).

With these models, we suggest the following scenario for the variation among SNe Ia: There exist some variations in the ignition conditions, such as the central density and temperature of the white dwarf, due to variations of the white dwarf age and the mass accretion rate. This would result in a difference in $v_{\rm def}$, which in turn leads to a somewhat larger difference in the density at the transition from deflagration to detonation. This results in a similar composition in the inner regions of (III) and (II), but a large variation of the composition in the outermost layer (I) such as in SN 1990N and SN 1991T. Cases like W7DN would be more common among SNe Ia, since the transition to detonation may occur more easily at lower densities because of smaller $v_{\rm CJ}/v_{\rm s}$ and larger $v_{\rm def}/v_{\rm s}$. Some variations in the expansion velocities of Si may be due to the variation of the transition density.

2.6 Discrimination of models

Figures 2.5 and 2.6 show the light curves of the most dominant γ-ray lines from the decay of ^{56}Ni (812 keV) and ^{56}Co (847 keV) based on the deflagration model W7 and the late detonation models W7DT, respectively (Kumagai *et al.* 1992 [38]). Obviously, the 812 keV line intensity emitted from ^{56}Ni differs drastically by each model in the early phase. So, as mentioned shortly in Section 3.2.3, the 812 keV line flux maximum from the ^{56}Ni decay depends on the ^{56}Ni distribution, thus being sensitive to the model, which is useful for model discrimination.

If we apply W7DT to SN 1991T, the distance to this supernova can be estimated as follows: The bolometric luminosity at maximum brightness of W7DT is 1.04×10^{43} erg s^{-1}, which gives $M_{\rm bol} = -18.73$ (Section 4). Taking $M_{\rm B} - M_{\rm bol} = -0.28$ and $m_{\rm B} = 11.20$ for the blue maximum of SN 1991T (BT92 [8]), we get 11.0 Mpc as a distance to SN 1991T.

Then the 847 keV line flux from the supernova is expected to be 4.3×10^{-5} photons cm^{-2} s^{-1} after 50 days.

The OSSE experiment on the COMPTON observatory has observed SN 1991T and obtained only the upper limit to the 847 keV γ-ray line flux as 4.4×10^{-5} photons cm^{-2} s^{-1} on $66 - 79$ days and 3.9×10^{-5} photons cm^{-2} s^{-1} on $176 - 190$ days (Lichti *et al.* 1992 [43]). This is marginally consistent with the predicted flux for W7DT. And if the observation of 812 keV γ-ray line will be made in the earlier phase for SNe Ia nearer than SN 1991T, we can determine how large amount of ^{56}Ni exists in the outermost region.

Chapter 3

Theoretical Light Curves

3.1 Radiative processes in supernovae

The light curve calculation for SNe Ia was performed by many investigators based on several explosion models. Woosley (1990) [84] gives some detonation and deflagration models and presents theoretical light curves based on them. Nomoto, Shigeyama (1991) [55] shows the light curves based on deflagration model W7 (see Section 2.2). The value of t_R of their light curves are $6 \sim 16$ days, because of relatively small optical opacity $\kappa_{\rm opt}$ (See Section 1.4.1).

In this Chapter, we present theoretical light curves based on the late detonation models. They will be compared with the observation of visual magnitudes of SNe 1990N and 1991T.

There are two steps in calculating the light curves of supernovae:

(I) Energy deposition.

The energy source of supernovae in their light maximum is the radioactive nuclei whose life time are the same order as the time at the light maximum from the explosion. Among them, ^{56}Ni and its daughter species ^{56}Co are thought to be the main source because they are the main products of (complete or incomplete) silicon burning and their half life periods are 6.6 days and 77 days, respectively. The emitted line γ-ray photons from their decays are degraded to soft X-ray by Compton scatterings. Then, these high energy electrons collide with electrons and ionizes ions or atoms. The ionized electrons are going the same way and finally thermalized. The energy from radioactive nuclei deposited in this way. And the energy deposited per unit time and mass will be called as deposition

function.

(II) Radiative transfer and the surface luminosity.

This radiation are transferred to the surface encountering many absorption / re-emission processes. These processes are bound - free reaction, bound - bound reaction, free - free transition (bremsstrahlung) and electron scattering. We get as the surface luminosity at some timing the photons whose source function is the deposited energy of that time, and then we can draw the light curves as the time sequence of the surface luminosity.

In next section, we treat (I) by two ways. (II) will be mentioned in the next chapter. The deflagration model W7 and the late detonation models introduced in Chapter 2 are used for the calculations. These models undergo the homologous expansion after few seconds from ignition.

3.2 Deposition function

3.2.1 Local absorption approximation

We estimate the effective opacity for the γ-ray photon emitted from radioactives such as ^{56}Ni or ^{56}Co on the same way as Shigeyama, Nomoto (1990) [69]. The γ-ray photon is scattered several times and lose its energy for each time. The total length that the γ-ray photon travels would be called 'effective' mean free path. This effective mean free path of the γ-ray photon is obtained as

$$l_\gamma = 1.67 \times 10^{13} (Y_e^T)^{-1} (\frac{\rho}{10^{-12}\mathrm{gcm}^{-3}})^{-1}\mathrm{cm}. \quad (3.1)$$

Here Y_e^T is the total number of free and bound electrons per nucleon. For the materials in SNe Ia, we can set $\sim$0.5 as this value, then the effective opacity becomes

$$\kappa_\gamma = (\rho l_\gamma)^{-1} = 0.03\mathrm{cm}^2\mathrm{g}^{-1}. \quad (3.2)$$

3.2.2 Monte Carlo simulations

This value of the deposited energy is also obtained by Monte Carlo simulations of X-ray transfer (Sutherland, Wheeler 1984 [73], Kumagai 1991 [37]). We now use the simulation

code presented in Kumagai (1991) [37] with $10^4 \sim 10^6$ random walk photons. This code is made to calculate the X or γ-ray light curves or spectra from supernovae, but at the same time we can get the deposited energy from line γ-ray, obviously. The supernova models are re-constructed to 28 shells of same mass, and in one shell the density and chemical composition are treated as uniform.

A part of this simulation is computed by the computer FACOM M780 at the Institute of Space and Astronautical Science.

3.2.3 The comparison of results

In Figures 3.1 to 3.3, the results obtained with these two methods using 3 models (W7, W7DT, W7DN) are shown. For the first $\sim$30 days, the deposition functions with these two methods basically coincide in every model. And, in the later stage, the deposition function with Monte Carlo simulation is smaller than that with constant κ_γ. This means that the approximation of κ_γ as constant is very good in early stage, and considering that the light maximum of SNe Ia comes about 20 days after explosion (see Section 1.4.1), this approximation is very useful for the estimation of the maximum luminosity of SNe Ia. Then, we can trust the previous results of light curve research with constant κ_γ (e.g. Shigeyama *et al.* 1992 [71] for instance). Monte Carlo simulation to get the deposition function takes 1 week or so on workstation and some hours even on main-frame computer, besides the calculation with constant opacity takes only some minutes on workstation, the parameter survey or preliminary calculation can be done with constant κ_γ.

The difference between the results with two methods in later phase can be understood as follows. In the later stage, the ejecta becomes very low density, so the number of times of Compton scattering per γ-ray photon would be decrease. As a consequence, effective mean free path l_γ grows and κ_γ decreases.

The deposition function of W7 model is almost the same as that of W7DN model and is smaller than that of W7DT model. This is the reflection of the amount of heat source ^{56}Ni, but the ratio of this amount and the difference in deposition function is somewhat different. The difference in deposition function between in W7 model and W7DT model is $\sim$ 10 per cent, though ^{56}Ni mass of W7DT model is 30 per cent larger than that of

W7 model. This can be explained by the location of additional ^{56}Ni in late detonation models. The heat sources produced by late detonation wave locates in the outermost region of ejecta, where density is very small compared with the central region. Then line γ-ray photon emitted from radioactive nuclei has indeed less chance to be scattered by electrons than that in inner region. The deposited energy in this region is very small rather than the amount of radioactive nuclei.

In other words, line γ-ray photons emitted in late detonation region easily escape from the ejecta without being scattered. So, we can decide which of deflagration model or late detonation model is real with the observation of line γ-ray from type Ia supernovae. This has been discussed in Section 2.6.

3.3 Method of light curve calculations

Light curves of the exploded white dwarfs are powered by the radioactive decay chain ^{56}Ni $\rightarrow$ ^{56}Co $\rightarrow$ ^{56}Fe. The original γ-ray energy is partly lost as γ-ray emissions and partly deposited in the ejecta through multiple Compton scatterings and the atomic processes. In this study, we use the rate of γ-ray energy deposition obtained by calculating with Monte Carlo simulation in Section 3.2.

For the optical light curve, radiative transfer is calculated with the flux-limited diffusion approximation (Shigeyama, Nomoto 1990 [69]) derived by Pomraning (1983) [64]. The radiative transfer equation to be solved is

$$\frac{1}{c}\frac{\partial I_\nu(\mathbf{r},t,\mathbf{\Omega})}{\partial t} + \mathbf{\Omega}\cdot\nabla I_\nu(\mathbf{r},t,\mathbf{\Omega}) = -(\kappa_\nu+\sigma_\nu)\rho(I_\nu(\mathbf{r},t,\mathbf{\Omega}) - B_\nu(\mathbf{r},t)), \tag{3.3}$$

where $I_\nu(\mathbf{r},t,\mathbf{\Omega})$ is the specific intensity of radiation at a position $\mathbf{r}$, time t, and in the direction $\mathbf{\Omega}$, κ_ν and σ_ν are respectively the absorptive and scattering opacities, and a correction for the induced emission is included in κ_ν. $B_\nu(\mathbf{r},t)$ is the Planck energy density per unit frequency.

We assume that the specific intensity $I_\nu(\mathbf{r},t,\mathbf{\Omega})$ is given as

$$I_\nu(\mathbf{r},t,\mathbf{\Omega}) = \Psi(\mathbf{\Omega})B_\nu(\mathbf{r},t), \tag{3.4}$$

where $\Psi(\mathbf{\Omega})$ is a function of $\mathbf{\Omega}$, independent of $\mathbf{r}$ and t. Substituting this expression into Equation 3.3 and its zeroth moment, and eliminating $\partial B_\nu(\mathbf{r},t)/\partial t$ from them, we obtain

$$\Psi = \frac{1}{1+\mathbf{f}\cdot\mathbf{R}_\nu/4\pi - \mathbf{\Omega}\cdot\mathbf{R}_\nu}. \tag{3.5}$$

Here the dimensionless flux $\mathbf{f}$ and the flux-limiting parameter $\mathbf{R}_\nu$ are defined as

$$\mathbf{f} = \int_{4\pi} d\mathbf{\Omega}\mathbf{\Omega}\Psi(\mathbf{\Omega}), \tag{3.6}$$

$$\mathbf{R}_\nu = -\nabla B_\nu(\mathbf{r},t)/\{(\kappa_\nu+\sigma_\nu)\rho B_\nu(\mathbf{r},t)\}. \tag{3.7}$$

Putting Equation 3.5 into Equation 3.6, and carrying out the integration about $\mathbf{\Omega}$, $\mathbf{f}$ is obtained as

$$\frac{\mathbf{f}}{4\pi} = \frac{\mathbf{R}_\nu}{R_\nu^2}(R_\nu\coth R_\nu - 1), \tag{3.8}$$

where $R_\nu = |\mathbf{R}_\nu|$. The flux $\mathbf{F}_\nu(\mathbf{r},\mathbf{t})$, defined as

$$\mathbf{F}_\nu(\mathbf{r},t) = \int_{4\pi} d\mathbf{\Omega}\mathbf{\Omega}I_\nu(\mathbf{r},t,\mathbf{\Omega}), \tag{3.9}$$

is written as

$$\mathbf{F}_\nu(\mathbf{r},\mathrm{t}) = 4\pi\frac{\mathbf{R}_\nu}{R_\nu^2}(R_\nu\coth R_\nu - 1)B_\nu(\mathbf{r},t). \tag{3.10}$$

To obtain the bolometric luminosity, we use the Rossland mean opacities in Equation 3.7 and integrate the Planck energy density over the photon frequency. Finally, we obtain the equation to calculate

$$\begin{aligned}\frac{\mathbf{L}}{4\pi r^2} &\equiv \int_0^\infty d\nu\mathbf{F}_\nu(\mathbf{r},\mathrm{t}) \\ &= \frac{\mathbf{R}}{R^2}(R\coth R - 1)4\sigma T^4.\end{aligned} \tag{3.11}$$

Here, $\mathbf{R} = -\nabla T^4/\{(\overline{\kappa}+\overline{\sigma})\rho T^4\}$, $R = |\mathbf{R}|$, σ the Stefan-Boltzmann constant, $\overline{\kappa}$ ($\overline{\sigma}$) the Rossland mean of κ_ν (σ_ν).

We have to estimate the opacity which consists of scattering and absorption. The scattering opacity, however, is negligible around the maximum light, because the temperature of ejecta is low and there are small number of free electrons. The same concept is held about the free-free absorption opacity. Then, we treat only the bound-free and

bound-bound absorption opacity as the optical opacity $\kappa_{\rm opt}$. The Rossland mean of them, however, is highly uncertain, especially in the atmosphere with a large velocity gradient. For simplicity, we assume that

$$\kappa_{\rm opt} = \overline{\kappa} + \overline{\sigma} = \text{constant}. \tag{3.12}$$

For the value of $\kappa_{\rm opt}$, we choose $\sim$ 0.3 (in units of cm^2 g^{-1} hereafter), with which t_R becomes $\sim$20 days based on W7 model (Shigeyama, Nomoto 1990 [69]). In order to fit to the observations, light curves with some other values are also investigated.

3.4 Light curves of deflagration models and late detonation models

The bolometric light curves of the late detonation model W7DN and W7DT are shown in Figures 3.4 and 3.5, respectively. To get the same $t_{\rm R}$ as W7, $\kappa_{\rm opt}$ is set to be 0.3 (0.35) for W7DN (W7DT) model. Compared with W7, $L_{\rm max}$ is slightly higher because of a larger ^{56}Ni mass, but the difference is remarkably smaller than that of the amount of heat source ^{56}Ni. This characteristics can be explained with that additional radioactive heat sources being located such outer and lower-density region that they do not play important contributions as the optical energy deposition at and after the maximum light (See also Chapter 3.2.3). Maximum brightness is reached when the expansion time scale becomes comparable to that of heat diffusion from the radioactive source. The light curve shape thus depends on the effective diffusion time $(\kappa_{\rm opt} M/v_{\rm exp} c)^{1/2}$ (Arnett 1982 [1]). Therefore $t_{\rm R}$ is smaller and thus the maximum luminosity $L_{\rm max}$ is higher for smaller $\kappa_{\rm opt}$ and higher $v_{\rm exp}$.

The outer heat source tends to lead the maximum light earlier. So, in order to get the same t_R, we should choose the larger $\kappa_{\rm opt}$ for W7DT model than for W7 or W7DN. And considering the expansion opacity, it would be natural that the late detonation model who has larger expansion velocity because of the additional nuclear burning get the larger effective optical opacity. This will be shortly discussed in next section.

On the other hand, the style of curve differs greatly: W7DN grows very earlier than W7. The γ-ray produced in late detonation region is scattered at this period because in

early phase the matter has rather high density and is ionized because of higher temperature than later.

After the peak, the bolometric luminosity gets closer to the energy deposition rate that decreases because of the increasing transparency of the ejecta to γ-rays as well as the decreasing number of radioactive elements. The calculated curve of the decline phase for every model are in reasonable agreement with the observed visual light curves (Figures 3.4 and 3.5).

3.5 Comparison with the observation of SNe 1990N and 1991T

The calculated curves are compared with the observed visual light curves of SNe 1990N and 1991T in Figures 3.4 (Leibundgut *et al.* 1991 [39], LTCC91 [41]) and 3.5 (Filippenko *et al.* 1992a [19]), where the observed maximum brightness is arbitrarily shifted to the calculated $L_{\rm max}$. It is seen that the light curves of W7DN and W7DT are both in reasonable agreement with the slow rise and blunt peak of SNe 1990N and 1991T, respectively.

Since the bolometric light curve is regarded to be close to the visual one, this agreement is encouraging for a further study, whether the explosion model has actually an expansion opacity as large as $\kappa \sim 0.3$ cm^2 g^{-1} on the average (Harkness 1991a [23]; Höflich *et al.* 1991 [26]; Khokhlov *et al.* 1991 [33]). Qualitatively speaking, W7DT would have larger $\kappa_{\rm opt}$ than W7 or W7DN because of larger amount of iron peak elements. This is consistent with the above estimation from the shape of calculated light curves. Then, we can expect that the maximum luminosities of SNe Ia are very identical even if the transition point from deflagration to detonation differ from each other. It will be discussed in Chapter 4.

Chapter 4

Application to Determine the Hubble Constant H_0

4.1 Observed maximum luminosities

The maximum brightness $L_{\rm max}$ of SNe Ia when explained with radioactive decay models has been used to estimate the Hubble constant H_0 (in units of km s^{-1} Mpc^{-1} hereafter). From the well-observed six SNe Ia, Arnett *et al.* (1985) [2] derived

$$L_{\rm bol,max} \sim 1.9 \pm 0.3 \times 10^{43} \left(\frac{H_0}{50}\right)^{-2} \ {\rm erg\ s^{-1}}. \tag{4.1}$$

Recently, Branch (1992) [6] has given the value of $M_{\rm B}(100)$, which is the SN Ia peak absolute blue magnitude for a Hubble constant of 100. With the bolometric correction $M_{\rm B} - M_{\rm bol} = 0.28 \pm 0.10$ (Branch 1992 [6]), we obtain

$$L_{\rm bol,max} \sim 2.06 \pm 0.28 \times 10^{43} \left(\frac{H_0}{50}\right)^{-2} \ {\rm erg\ s^{-1}}. \tag{4.2}$$

Hereafter we use this equation to derive the Hubble constant.

4.2 Theoretical maximum luminosities

In the radioactive decay models of the light curve, the rise time to maximum light $t_{\rm R}$ depends on the optical opacity $\kappa_{\rm opt}$; for larger $\kappa_{\rm opt}$, $t_{\rm R}$ is longer. Unfortunately the opacity is subject to a rather large uncertainty, so that we have calculated the light curve for several values of $\kappa_{\rm opt}$ (Section 3.3, 3.4). Figure 4.1 shows how the theoretical $L_{\rm max}$ ($L_{\rm max,th}$) depends on $t_{\rm R}$. For longer $t_{\rm R}$, $L_{\rm max,th}$ is lower because $L_{\rm max,th}$ is close to the

deposited radioactive luminosity at maximum light which decreases with time. Figure 4.1 also shows that $L_{\rm max,th}$ of W7 and W7DN are almost identical and that of W7DT is also very close for $t_{\rm R} > 18$ d (Section 3.4). The empirical relation between $L_{\rm max,th}$ and $t_{\rm R}$ is expressed as

$$L_{\rm max,th}/(1 \times 10^{43}\ {\rm erg\ s^{-1}}) = -0.068\, t_{\rm R} + 2.11 \tag{4.3}$$

for 17 d $< t_{\rm R} <$ 21 d.

Recent discovery of SNe Ia (SN 1990N) well before the maximum leads to longer $t_{\rm R}$ ($\sim$ 20 d) than the previous estimate ($\sim$ 16 d). In view of the similarity of the light curve of SN 1990N and other SNe Ia, $t_{\rm R} \sim 20$ d seems to be common to most of type Ia supernovae. Therefore, we take $t_{\rm R} = 19 \pm 2$ d (Branch 1992 [6]).

4.3 The Hubble constant H_0

By comparing the calculated $L_{\rm max,th}$ given in Figure 4.1 with the observed $L_{\rm max}$, H_0 is given as a function of $t_{\rm R}$ in Figure 4.2. If we take $t_{\rm R} = 19 \pm 2$ d as estimated from the observations, $H_0 = 2.3\ t_{\rm R} + 29.7$. The relation of Equation 4.2 is used for Figure 4.2.

If we take W7 and $t_{\rm R} = 19 \pm 2$ d for the best estimates, we obtain

$$H_0 = 73 \pm 10. \tag{4.4}$$

This is somewhat larger than the previous estimate based on the white dwarf explosion model ($\sim 60 \pm 10$: Branch 1992 [6]), because we adopt longer $t_{\rm R}$ and our light curve models are in better agreement with the observations.

In reproducing the observed spectra of SNe Ia, models with the Ni mass of 0.5 $M_\odot$ (model C6 in NTY [59]) and 0.7 $M_\odot$ (model W8 in NTY [59]) are marginally consistent (Harkness 1991b [24]). The Ni mass depends on the carbon ignition density and metallicity because more neutron-rich environment (due to larger electron capture and larger ^{22}Ne abundance) leads to the production of smaller mass ^{56}Ni. For example, for lower (larger) metallicity, larger (smaller) Ni mass is obtained because of smaller (larger) neutronization. To provide a possible range of uncertainties, we calculate the light curve for $M_{\rm Ni} = 0.5\ M_\odot$ (W75) and 0.7 $M_\odot$ (W77) where the hydrodynamical model is the same as W7 but the central iron-peak elements such as ^{54}Fe, ^{56}Fe, ^{58}Ni are artificially converted into ^{56}Ni and

vice versa. The results are shown in Figure 4.2, where luminosity scales approximately as $M_{\rm Ni}^{-1/2}$. If we include these uncertainties, we obtain $H_0 = 74 \pm 16$.

Our value of $H_0 = 73 \pm 10$ tends to be smaller than 80 ± 10 obtained from the luminosity functions of planetary nebulae (PNLF: Jacoby, Ciardullo, Ford, 1990 [28]) and 82 ± 7 by using the fluctuation of the surface brightness of galaxies (Tonry, 1991 [78]), but could be compatible with those values within a reasonable error bar.

Expanding photosphere method (EPM) with type II supernovae (Schmidt, Kirshner, Eastman 1992 [67]) has given $H_0 = 60 \pm 10$, which has recently been revised to be 67 ± 10. (If Virgo infall correction is included, H_0 would be larger.) This is compatible with our estimate.

Most recent observational estimation of the absolute peak magnitude of SN Ia (see Page 8) gives that $H_0 = 51 \pm 10$ (Sandage *et al.* 1992 [66]). Discrimination whether this SN Ia 1937C was exceptionally bright need more investigation.

Chapter 5

Conclusion

I. We have shown that some variation of the spectroscopic and photometric features of SNe Ia as observed in SN 1990N and SN 1991T can be accounted for by introducing a late detonation model into the standard carbon deflagration model. The late detonation model assumes that the central carbon deflagration is transformed into detonation near the surface in some case of thermonuclear explosions and can account for the variation of the composition features. We suggest that the best way to test the model is to observe the line γ-rays from the decay of ^{56}Ni well before the optical maximum.

II. We have calculated theoretical light curves of the late detonation models as well as the carbon deflagration model with an improved energy deposition function obtained from the Monte Carlo simulation. The calculated light curves are in good agreement with the observed light curves if the optical opacity $\kappa_{\rm opt}$ is somewhat larger than previously considered.

III. We have estimated the Hubble constant by comparing the theoretical light curve with the observed light curve of SNe Ia. Our estimate is $H_0 = 73 \pm 10$, which is somewhat larger than that previously estimated from SNe Ia. Our result is compatible with the estimation with other methods.

Appendix A

Models for Peculiar Type Ia Supernovae — Explosion of a C+O Star

A.1 Peculiar SN Ia 1991bg

SN 1991bg in NGC 4374 (M84) which is a member of the Virgo cluster was discovered by Reiki Kushida at Yatsugatake South Base Observatory on December 9.844UT, 1991 (Kosai, 1991 [36]). Because the host galaxy is elliptical and a spectroscopy of this object shows the strong Si II absorption line (Kirshner, 1991 [35]), SN 1991bg is classified as type Ia.

Afterwards, however, some peculiarities of this supernova have been pointed out. The peak V magnitude of SN 1991bg was about 14 mag (see Figure A.1), being much dimmer than the mean peak V magnitude (∼12 mag (BT92 [8])) of SNe Ia appears in the Virgo cluster. The light curve feature, especially in the decline phase, is steeper than normal SNe Ia. In addition, the host galaxy NGC4374 have produced another SN Ia 1957B, whose peak V magnitude is 12.5 (LTCC91 [41] and see Figure A.1) and is normal for the Virgo type Ia. (This is an exception of the peak luminosity homogeneity discussed in Page 7.) This shows that the maximum brightness of SN 1991bg is one forth of that of SN1957B. Then, this supernova is thought to be peculiar type Ia, or should be classified as other type.

Some of researchers attempt to explain this peculiarity as is caused by absorption due to the interstellar medium in the host galaxy, same as 1986G in NGC 5128

(Cen A). Phillips and Hamuy (1991) [62] shows that there is no narrow Na I D absorption line due to interstellar medium in the spectra of SN 1991bg. Filippenko *et al.* (1992b) [20] gives the same observational results and concludes that this supernova is really subluminous. Filippenko *et al.* (1992b) [20] also shows that there exist O I absorption lines in the spectra of SN 1991bg near the maximum light and absorption lines due to Fe are relatively weak.

These observational feature mentioned above is very difficult to be illustrated on the basis of write dwarf explosion models. We propose other possible model which is the explosion of a massive star whose hydrogen and helium envelope is lost by the mass exchange in contact binary system.

A.2 The origin of a C+O star

Yamaoka, Shigeyama, Nomoto (1992) [89] investigate the origin of double neutron star systems discovered as binary pulsars whose companion star is regarded to be also a neutron star. They present the scenario that double neutron star system is the last evolutionary stage of the massive star binary.

They assume that double neutron star systems are formed through the following evolutionary stages (e.g., van den Heuvel 1987 [81]; Bhattacharya and van den Heuvel 1991 [5] and references therein):

(1) a binary system composed of two main-sequence stars 1 and 2,

(2) Roche lobe overflow of star 1, which becomes a helium star 1,

(3) the first supernova explosion of helium star 1 to form a neutron star 1,

(4) Roche lobe overflow of star 2, which leads to a spiral-in of neutron star 1 into star 2 and thus to a considerable shrink of the system due to losses of angular momentum and mass from the system; the system now consists of a recycled neutron star 1 and a helium star 2 in circular orbits, and

(5) the second supernova explosion of star 2; this forms a two neutron star system in eccentric orbits.

There are two possible scenarios for the explosion to form neutron star 2:

(a) Star 2 is a helium star of more massive than $\sim 5M_\odot$ (i.e., $\gtrsim 18\ M_\odot$ on the main-sequence). Smaller mass stars have too large radii to be accommodated in the Roche lobe.

(b) Star 2, being a helium star of smaller than 5 $M_\odot$ at its early phase, expands to lose its helium envelope by Roche lobe overflow and becomes an almost bare C+O star. The masses of C+O stars are 6.0, 3.8, 2.1, and 1.8 $M_\odot$ for M_α = 8, 6, 4, 3.3 $M_\odot$, respectively (Nomoto and Hashimoto 1988 [53]).

In order to survive as a binary system, the explosion of star 2 cannot be spherical, imparting a large kick velocity to the newly born neutron star, if star 2 has large mass at explosion. The first scenario (a) of the asymmetric explosion of helium stars requires the kick velocity as large as several hundreds km/s.

For the second scenario (b), Roche lobe overflow of helium star 2 ($M_\alpha \lesssim 5$ $M_\odot$) would lead to a spiral-in of neutron star 1 into helium star 2. Losses of mass and angular momentum from the system would significantly reduce the separation between C+O star 2 and neutron star 1. The resulting separation may well be smaller than those observed, though the estimation of angular momentum loss needs a more quantitative study. For this reason, the helium star scenario (a) would be favored for making the *observed* double neutron star systems.

However, a double neutron star system formed through the C+O star scenario (b) may not be rare. Especially, a Be/X-ray binary is expected to form a system consisting of a neutron star and a helium star with $M_\alpha \lesssim 5\ M_\odot$ (e.g., Bhattacharya and van den Heuvel 1991 [5] for a review). If this is the case, a double neutron star system with much shorter orbital period than ever observed should be discovered in future. If no such systems could be discovered, it would imply that the spiral-in of the neutron star into the Be star does not take place due to earlier mass loss (e.g., Bailes 1989 [4]) or the spiral-in of the neutron star into the low mass helium star leads to entirely different system as a result of merging.

Explosions of C+O stars might be observed as SNe Ic because the stars do not contain hydrogen or helium. The progenitor's small mass may be consistent with a fast decline of SN Ic light curves (Filippenko *et al.* 1990 [18]; Nomoto *et al.* 1990 [51]). However, the complete absence of hydrogen in C+O stars is not consistent with the presence of a tiny amount of hydrogen observed in some SNe Ic (Jeffery *et al.* 1991 [30]; Filippenko 1992 [17]). Because of the smaller mass of heat source ^{56}Ni than white dwarf burning, the exploding C+O stars might be easily missed or observed as some peculiar SNe Ia.

A.3 Explosion model and light curve calculation

To construct a presupernova C+O star, we cut out a C+O core from the helium star model (Hashimoto *et al.* (1992) [25]) and attach a small polytropic envelope with index 3. We choose the models whose M_α = 5.0, 4.0, 3.3 $M_\odot$, and thus $M_{\rm C+O}$ = 2.9, 2.1, 1.8 $M_\odot$, respectively. The composition structures of those models are shown in Figures A.2 to A.4. These masses are corresponding to the main-sequence mass of 18, 15, 13 $M_\odot$, respectively.

The explosion of star 2 is caused by gravitational collapse and there remains a neutron star. There exists a mass cut, interior to which collapses to neutron star and outer than which is ejected and burned with explosive nucleosynthesis. The point of mass cut is uncertain, but we assumed that the C+O stars of 2.9, 2.1, and 1.8 $M_\odot$ form neutron stars of masses 1.4, 1.28, and 1.2$M_\odot$ (model CO2.9, CO2.1, and CO1.8), respectively, whose values are taken from Hashimoto *et al.* (1992) [25].

A hydrodynamical models of supernova explosion and associated explosive nucleosynthesis are calculated in the same way as has been done for SN 1987A (Shigeyama and Nomoto 1990 [69]). The explosive nucleosynthesis calculation is performed with an energy generation network including 13 nuclear species as described in section 2.2. The final kinetic energy are assumed to be 10^{51} erg for each model, which is same order as that of SN 1987A (e.g., Nomoto *et al.* 1991 for a review).

For the light curve calculation, radiative transfer code introduced in Section 3.3

is also used. The deposited energy from ^{56}Ni and ^{56}Co is obtained with constant γ-ray absorption coefficient of κ_γ as 0.03 cm^2 g^{-1}. In order to compare with the light curve based on W7 (Section 3.3), a constant optical opacity of $\kappa_{\rm opt}$ is set to be 0.3.

A.4 Results

The calculated chemical compositions versus mass and expansion velocity for CO2.9, CO2.1, and CO1.8 are shown in Figures A.5 $\sim$ A.7 and the masses of 13 species elements of the explosion models is summarized in Table A.1 with those of W7. The main characteristics of nucleosynthesis in the C+O stars, compared with W7, are as follows;

a) The mass fraction of oxygen in the ejecta is larger.

b) The mass fraction of silicon is smaller.

c) Produced ^{56}Ni amount is smaller.

d) The expansion velocities of the Si layers are of the same in W7 and CO2.9 but larger in CO2.1 and CO1.8.

Among them, d) is due to employment the same kinetic energy 1.0 $\times 10^{51}$ erg for both of CO2.9 and CO1.8 arbitrarily. The first half of c) is consistent with the results of Shigeyama *et al.* (1990) [70] which showed that the explosion of the less massive helium star produces more ^{56}Ni. But this includes the large uncertainty: the point of mass cut. The quantitative discussion about the amount of ^{56}Ni should be done after the explosion energy and the point of mass cut will be explained as the function of initial helium star mass (or C+O star mass). But it would be true that C+O star explosion produces less ^{56}Ni than the explosion of white dwarf, and that the white dwarf explosion is much brighter than that of C+O star.

The deposition functions and bolometric light curves based on CO2.9, CO2.1, and CO1.8 are shown in Figure A.9. Those of W7 is also presented for comparison. The maximum luminosity of CO2.9 is about one seventh (2.2 mag fainter) than that

of W7. And $t_{\rm R}$ for CO2.9 is about 35 days with a gentle-sloping light curve. The low maximum luminosity is the consequence of small ^{56}Ni mass, obviously. And the gentleness of light curve is caused by small $E_{\rm kin}/M_{\rm ej}$, where $E_{\rm kin}$ is the total kinematic energy of ejected mass and $M_{\rm ej}$ reveals the mass of ejecta.

The shape of the light curves of CO2.1 and CO1.8 are steeper than that of CO2.9. This is a consequence of the larger $E_{\rm kin}/M_{\rm ej}$. Their peak luminosity is some larger and their $t_{\rm R}$ is smaller than that of CO2.9. Brighter luminosities are consequent of larger ^{56}Ni, and because smaller $M_{\rm ej}$ make total optical thickness smaller, the maximum lights come earlier and decline rates goes larger.

For comparison, the light curve based on the explosion model of 2.9 $M_\odot$ C+O star whose $E_{\rm kin}$ is 1.4 $\times 10^{51}$ erg (CO2.9B) is shown in Figure A.10 with that of CO2.9. And the composition structure of CO2.9B is presented in Table A.1 and Figure A.8, too. Model CO2.9B has the same mass cut (1.4 $M_\odot$) as model CO2.9, but the total ^{56}Ni mass of CO2.9B is larger than CO2.9 because of more explosive nucleosynthesis with larger energy input at mass cut. The shape of the light curve based on CO2.9B is sharper than that of CO2.9 because of larger $E_{\rm kin}/M$ej. And $t_{\rm R}$ for CO2.9B is about 30 days. Conclusively, the shape or $t_{\rm R}$ with this scenario changes depending on the location of mass cut (i.e. mass of remained neutron star) and $E_{\rm kin}$ (namely, the input energy at mass cut point).

A.5 Comparison with observation

A.5.1 Application to SN 1991bg

The spectral features of SN 1991bg (see Section A.1) are qualitatively consistent with the C+O star models. A large amount of oxygen would not be ejected by white dwarf explosion. And C+O star explosion is always subluminous comparing with (whole) white dwarf explosion because of small amount of ^{56}Ni. In addition, the light curve with C+O star explosion model is fittable for observation if we take some small $M_{\rm ej}$ and/or some large $E_{\rm kin}$.

Figure A.11 shows the bolometric light curve of CO1.8 with the observed light curve of SN 1991bg (Leibundgut *et al.* 1992 [42]). The observational maximum light is arbitrarily shifted to fit to the calculated one. These two make remarkable coincidence at the maximum light and in the later phase. And the peak brightness of CO1.8 is about one third of that of W7, which is consistent between SN 1991bg and SN 1957B.

The ejected mass from C+O star explosion is relatively small ($0.6 \sim 1.5\ M_\odot$). With the ejecta of mass $0.6\ M_\odot$, low peak luminosity and fast decline observed in SN 1991bg are able to be explained. Applying this relation to the white dwarf explosion model, the ejected mass have to be $\sim 0.6\ M_\odot$, in order to figure out the characteristics of SN 1991bg. As mentioned in Filippenko *et al.* (1992b) [20], the partial explosion of white dwarf would be possible, also.

This scenario for SN 1991bg has a serious difficulty: since the host galaxy is elliptical, the massive stars would have ended their life long ago. Since the light curve model which is fit to the observed light curve of SN 1991bg would have small mass (small $M_{\rm ej}$), it is possible that this is one of the last explosion of massive stars in NGC 4374.

A.5.2 Discrimination the C+O star explosion from white dwarf explosion

The ejecta from the explosion of the C+O star contain a large amount of oxygen. This oxygen is produced at the later stage of stellar evolution, which made the C+O layer by helium burning and O+Ne+Mg layer by carbon burning. And the explosive nucleosynthesis at the moment of supernova explosion occurs mainly in Si layer, these oxygen would be ejected without burning. This is common feature among the supernovae caused by gravitational collapse.

Since the outer hydrogen or helium envelope does not exist for the C+O star, the oxygen absorption feature can be seen at the earlier phase than typical type II supernovae. And also, the mixing caused by Rayleigh-Taylor instability is likely to

occur for this explosion since there is composition jump besides white dwarf burning has no composition structure inner than (fresh) accreted matter naturally. Then, the synthetic spectra with this model is urged, and now we are planning to obtain it.

Appendix B

Deceleration Parameter q_0

Equation 4.2 is the transformation from the equation that reveals the line in Hubble diagram presented in Page 7. Equation 4.2 is obtained by

$$m_{\max} - M_{\max} = 5\log(\frac{cz}{H_0}) \tag{B.1}$$

with $m_{\max} = 12.0 \pm 0.2$ mag at $z = 0.003$. This is indeed the Hubble's law.

But Equation B.1 is only an approximation for the region of $z \ll 1$. For $z \sim 1$,

$$m_{\max} - M_{\max} = 5\log(\frac{cz}{H_0}) - 1.086(1 - q_0)z, \tag{B.2}$$

where q_0 is the deceleration parameter, is available instead of Equation B.1.

Recently, very distant SN Ia 1992bi is discovered during a search for high-redshift supernovae with the Isaac Newton 2.5 m telescope (Pennypacker *et al.* 1992 [61]). The redshift of the host galaxy is 0.457, and SN 1992bi is detected at R = 22 mag. If this search will discover several SNe Ia at $z \sim 0.5$, we can estimate not only the Hubble constant H_0 but also the deceleration parameter q_0. The estimation of $m_{\max}$ for distant type Ia supernovae at $z \sim 0.5$ is performed with the accuracy of 0.1 mag, we would be able to distinguish whether $q_0 = 1.0$ or $q_0 = 0.5$. Note, the estimation of q_0 demands only the homogeneity of SNe Ia and does not require the maximum absolute luminosity.

Bibliography

[1] Arnett, W.D. 1982, *Astrophys. J.*, **253**, 785

[2] Arnett, W.D., Branch, D., Wheeler, J.C. 1985, *Nature*, **314**, 337

[3] Axelrod, T. 1980, in *Type Ia Supernovae*, ed. J.C. Wheeler (Univ. of Texas), p. 80

[4] Bailes, M. 1989, *Astrophys. J.*, **342**, 917

[5] Bhattacharya, D., van den Heuvel, E.P.J. 1991, *Phys. Rep.*, **203**, 1

[6] Branch, D. 1992, *Astrophys. J.*, **392**, 35

[7] Branch, D., Doggett, J.B., Nomoto, K., Thielemann, F.-K. 1985, *Astrophys. J.*, **294**, 619

[8] Branch, D., Tammann, G.A. 1992, *Ann. Rev. Astron. Astrophys.*, in press (BT92)

[9] Branch, D., Venkatakrishna, K.L. 1986, *Astrophys. J. Lett.*, **306**, L21

[10] Cadonau, R., Sandage, A., Tammann, G.A. 1985, in *Supernovae as Distance Indicators*, ed. N. Bartel (Lect. Notes. Phys. 224), p. 151

[11] Canal, R., Garcia, D., Isern, J., Labay, J. 1990, *Astrophys. J. Lett.*, **356**, L51

[12] Capaccioli, M., Cappellaro, E., Della Valle, M., D'Onofrio, M., Rosino, L., Turatto, M. 1990, *Astrophys. J.*, **350**, 110

[13] Clark, D.H., Stephenson, F.R. 1977, *The Historical Supernovae*, Oxford: Pergamon Press

[14] Clark, D.H., Stephenson, F.R. 1982, in *Supernovae: A Survey of Current Research*, eds. M.J. Ress, R.J. Stoneham (Dordrecht: Reidel), p. 355

[15] Croswell K. 1992, *New Scientist*, 18 July, 16

[16] Della Valle, M., Panagia, N. 1992, preprint

[17] Filippenko, A.V. 1992, *Astrophys. J. Lett.*, **384**, L73

[18] Filippenko, A.V., Porter, A.C., Sargent, W.L.W. 1990, *Astron. J.*, **100**, 1575

[19] Filippenko, A.V., Richmond, M.W., Matheson, T., Shields, J.C., Burbidge, M, Cohen, R.D., Dickinson, M., Malkan, M.A., Nelson, B., Pietz, J., Schlegel, D., Schmeer, P., Spinrad, H., Steidel, C.C., Tran, H.D., Wren, W. 1992a, *Astrophys. J. Lett.*, **384**, L15

[20] Filippenko, A.V., Richmond, M.W., Branch, D., Gaskell, C.M., Herbst, W., Ford, C.H., Treffers, R.R., Matheson, T., Ho, L.C., Dey, A., Sargent, W.L.W., Small, T.A., van Breugel, W.J.M. 1992b, *Astron. J.*, **104**, 1543

[21] Gilmore, G. 1989, in *The Milky Way as a Galaxy*, eds. G. Gilmore, I. King, P. van der Kruit, Geneva Obs., p. 227

[22] Graham, J.R. 1987, *Astrophys. J.*, **315**, 588

[23] Harkness, R.P. 1991a, in *SN 1987A and Other Supernovae*, ed. I.J. Danziger (Garching: ESO), p. 447

[24] Harkness, R.P¿ 1991b, in *Supernovae*, ed. S.E. Woosley (New York: Springer), p. 454

[25] Hashimoto, M., Nomoto, K., Tsujimoto, T., Thielemann, F.-K. 1992, in *Nuclei in the Cosmos*, in press

[26] Höflich, P., Khokhlov, A.M., Müller, E. 1991, *Astron. Astrophys*, in press.

[27] Hoyle, F., Fowler, W.A. 1960, *Astrophys. J.*, **132**, 565

[28] Jacoby, G.H., Ciardullo, R., Ford, H.C. 1990, *Astrophys. J.*, **356**, 332

[29] Jeffery, D., Branch, D., Filippenko, A.V., Nomoto, K. 1991, *Astrophys. J. Lett.*, **377**, L89

[30] Jeffery, D.J., Leibundgut, B., Kirshner, R.P., Benetti, S., Branch, D., Sonneborn, G. 1992, *Astrophys. J.*, submitted

[31] Khokhlov, A.M. 1991a, *Astron. Astrophys.*, **245**, 114

[32] Khokhlov, A.M. 1991b, *Astron. Astrophys.*, **245**, L25

[33] Khokhlov, A.M., Müller, E., Höflich, P. 1991, *Astron. Astrophys.*, submitted.

[34] Kikuchi, S., *et al.* 1992, in preparation

[35] Kirshner, R. 1991, *IAU Circ. No.* 5403

[36] Kosai, H. 1992, *IAU Circ. No.* 5400

[37] Kumagai, S. 1991, Ph. D. Thesis, University of Tokyo

[38] Kumagai, S., Nomoto, K., Shigeyama, T., Yamaoka, H. 1992, in preperation

[39] Leibundgut, B., Kirshner R.P., Filippenko, A.V., Shields, J.C., Foltz, C.B., Phillips, M.M., Sonneborn, G. 1991, *Astrophys. J. Lett.*, **371**, L23

[40] Leibundgut, B., Tammann, G.A. 1990, *Astron. Astrophys.*, **230**, 81

[41] Leibundgut, B., Tammann, G.A., Cadonau, R., Cerrito, D. 1991, *Astron. Astrophys. Suppl.*, **89**, 537

[42] Leibundgut, B., Kirshner, R.P., Phillips, M.M., Wells, L.A., Suntzeff, N.B., Hamuy, M., Schommer, R.A., Walker, A.R., Gonzalez, L., Ugarte, P., Williams, R.E., Williger, G., Gomez, M., Marzke, R., Schmidt, B.P., Whitney, B., Caldwell, N., Peters, J., Chaffee, F.H., Foltz, C.B., Rehner, D., Siciliano, L., Barnes, T.G., Cheng, K.-P., Hintzen, P.M.N., Kim, Y.-C., Maza, J., Parker, J.Wm., Porter, A.C., Schmidtke, P.C., Sonneborn, G. 1992, *Astrophys. J.*, in press

[43] Lichti G., *et al.* 1992, *Astron. Astrophys. Suppl.*, in press

[44] Livne, E. 1990, *Astrophys. J. Lett.*, **354**, L53

[45] Lucy, L.B. 1991, *Astrophys. J.*, **383**, 308

[46] Maury, D.L., Thouvenot, E., Buil, C., Brunetto, L., Phillips, M.M. 1990, *IAU Circ.*, No. 5039

[47] Nomoto, K. 1982a, *Astrophys. J.*, **253**, 798

[48] Nomoto, K. 1982b, *Astrophys. J.*, **257**, 780

[49] Nomoto, K. 1986, *Ann. NY Acad. Sci.*, **470**, 294

[50] Nomoto, K. 1987, in *IAU Symposium 125, The Origin and Evolution of Neutron Stars*, eds. D.J. Helfand, J.-H. Huang (Dordrecht: Reidel), p. 281

[51] Nomoto, K., Filippenko, A.V., Shigeyama, T. 1990, *Astron. Astrophys.*, **240**, L1

[52] Nomoto, K., Hashimoto, M. 1987, *Ap. Space Sci.*, **131**, 395

[53] Nomoto, K., Hashimoto, M. 1988, *Phys. Rep.*, **163**, 13

[54] Nomoto, K., Kondo, Y. 1991, *Astrophys. J. Lett.*, **367**, L19

[55] Nomoto, K., Shigeyama, T. 1991, in *Supernovae*, ed. S.E. Woosley (New York: Springer), p. 572

[56] Nomoto, K., Shigeyama, T., Kumagai, S., Yamaoka, H. 1991, in *Supernovae and Stellar Evolution*, eds. A. ray and T. Velusamy (World Scientific), p. 116

[57] Nomoto, K., Sugimoto, D. 1977, *Pub. Astr. Soc. Japan*, **29**, 765

[58] Nomoto, K., Sugimoto, D., Neo, S. 1976, *Ap. Space Sci.*, **39**, L37

[59] Nomoto, K., Thielemann, F.-K., Yokoi, K. 1984, *Astrophys. J.*, **286**, 644 (NTY)

[60] Nomoto, K., Yamaoka, H., Shigeyama, T., Kumagai, S., Tsujimoto, T. 1992, in *Supernovae (Les Houches, Session LIV)*, eds. J. Audouze *et al.* (Elsevier Sci. Publ.), in press

[61] Pennypacker, C., Perlmutter, S., Goldhader, G., Goobar, A., Desai, J., Kim, A, Kim, M., Muller, R., Newberg, H., Small, I., Boyle, B., McMahon, R., Bunclark, P., Carter, D., Irwin, M., Terlevich, R., Ellis, R., Couch, W. 1992, *IAU Circ. No.* 5652

[62] Phillips, M.M., Hamuy, M. 1991, *IAU Circ. No.* 5408

[63] Phillips, M.M., Wells, L.A., Suntzeff, N.B., Hamuy, M., Leibundgut, B., Kirshner, R.P., Foltz, C.B. 1992, *Astron. J.*, in press

[64] Pomraning, G.C. 1983, *Astrophys. J.*, **266**, 841

[65] Ruiz-Lapuente, P., Cappellaro, E., Turatto, M., Gouiffes, C., Danziger, I.J., Della Valle, M., Lucy, L.B. 1992, *Astrophys. J. Lett.*, in press

[66] Sandage, A., Saha, A., Tammann, G., Panagia, N., Macchetto, F., 1992, *Astrophys. J. Lett.*, **401**, L7

[67] Schmidt, B.P., Kirshner, R.P., Eastman, R.G. 1992, *Astrophys. J.*, **395**, 366

[68] Schwarzschild, B. 1992, *Physics Today*, November 1992, 17

[69] Shigeyama, T., Nomoto, K. 1990, *Astrophys. J.*, **360**, 242

[70] Shigeyama, T., Nomoto, K., Tsujimoto, T., Hashimoto, M., 1990, *Astrophys. J. Lett.*, **361**, L23

[71] Shigeyama, T., Nomoto, K., Yamaoka, H., Thielemann, F.-K. 1992, *Astrophys. J. Lett.*, **386**, L13

[72] Strom, R.G. 1988, *Mon. Not. Roy. Astr. Soc.*, **230**, 331

[73] Sutherland, P., Wheeler, J.C. 1984, *Astrophys. J.*, **280**, 282

[74] Tammann, G.A., Leibundgut, B. 1990, *Astron. Astrophys.*, **236**, 9

[75] Thielemann, F.-K., Hashimoto, M., Nomoto, K. 1990, *Astrophys. J.*, **349**, 222

[76] Thielemann, F.-K., Jeffery, D.J., Nomoto, K., Yamaoka, H., Shigeyama,T. 1992, in preparation

[77] Thielemann, F.-K., Nomoto, K., Yokoi, K. 1986, *Astron. Astrophys*, **158**, 17

[78] Tonry, J.L. 1991, *Astrophys. J. Lett.*, **373**, L1

[79] van den Bergh, S. 1989, *Astron. Astrophys. Rev.*, **1**, 111

[80] van den Bergh, S. 1992, *Publ. Astron. Soc. Pacific*, **104**, 861

[81] van den Heuvel, E.P.J. 1987, in *IAU Symposium 125, The Origin and Evolution of Neutron Stars*, ed. D.J. Helfand and J.-H. Huang, Kluwer, Dordrecht, p. 393

[82] Waagan, E., Knight, S., Evans, R.O., Villi, M., Cortini, G., Johnson W., McNaught, R.H., Müller, J. 1991, *IAU Circ. No.* 5239

[83] Williams, F.A. 1985, *Combustion Theory* (Menlo Park: Benjamin / Cummings), p. 217

[84] Woosley, S.E. 1990, in *Supernovae*, ed. A.G. Petschek (New York: Springer), p. 182

[85] Woosley, S.E., Weaver, T.A. 1986a, *Lecture Notes in Physics*, **255**, 91

[86] Woosley, S.E., Weaver, T.A. 1986b, *Ann. Rev. Astron. Astrophys.*, **24**, 205

[87] Woosley, S.E., Weaver, T.A. 1992, in *Supernovae (Les Houches, Session LIV)*, eds. J. Audouze *et al.* (Elsevier Sci. Publ.), in press

[88] Yamaoka, H., Nomoto, K., Shigeyama, T., Thielemann, F.-K. 1992a, *Astrophys. J. Lett.*, **393**, L55

[89] Yamaoka, H., Shigeyama, T., Nomoto, K. 1992, *Astron. Astrophys.*, in press

Acknowledgement

The author would like to thank his adviser, Prof. Ken'ichi Nomoto for offering him the fascinating theme about supernovae. Without his continuous and persevering support and encouragement, this work can not be completed. He also thanks Professor Masaaki Hashimoto for helpful suggestion in Kyushu University. He is grateful to Prof. Friedrich-Karl Thielemann, Dr. Toshikazu Shigeyama, and Dr. Shiomi Kumagai for collaboration and helpful discussion. And he is also grateful to Prof. Yoji Osaki, Prof. Hideyuki Saio, Prof. Mariko Kato and Prof. Yoshiharu Eriguchi for continuous encouragement.

He wishes to thank Prof. Sadanori Okamura and Dr. Mamoru Doi for the valuable discussion about estimation of the Hubble constant.

Transition Point ($M_\odot$)	$M_{\rm Ni}$ ($M_\odot$)		$M_{\rm Si}$ ($M_\odot$)		$v_{\rm exp,Trans.}$ ($\times 10^9$cm/s)	
	deflag.	late deto.	deflag.	late deto.		
0.82	0.79	0.45	0.00	0.03	0.80	
0.94	0.87	0.32	0.02	0.04	1.01	
1.00	0.85	0.25	0.06	0.05	1.09	
1.08	0.83	0.16	0.08	0.05	1.20	(W7DT)
1.18	0.83	0.06	0.18	0.06	1.34	
1.20	0.82	0.03	0.18	0.06	1.37	(W7DN)
1.24	0.82	0.00	0.18	0.00	1.41	

Table 2.1: The mass of produced elements in deflagration and late detonation zones calculated with 13 species nucleosynthesis code. The real amount of ^{56}Ni would be some smaller than $M_{\rm Ni}$ presented in this table, because of central neutronization due to electron capture.

Model	Trans. point($M_\odot$)	$M_{\rm Ni,in}(M_\odot)$	$M_{\rm Ni,out}(M_\odot)$	$M_{\rm Si,in}(M_\odot)$	$M_{\rm Si,out}(M_\odot)$
W7	—	0.59	—	0.15	—
W7DN	1.20	0.59	0.04	0.14	0.06
W7DT	1.08	0.59	0.18	0.10	0.04
W8DT	1.26	0.70	0.09	0.11	0.01
W7DHE	1.20	0.59	0.13	0.16	0.00

Table 2.2: The summarized table of characteristics of deflagration and late detonation models. The mass of ^{56}Ni and Si produced in deflagration (notation in) and late detonation regions (notation out) are presented separately. These results are obtained by detailed nucleosynthesis calculation with 299 species.

element	total	$M_{\rm r} \leq 1.08$	$M_{\rm r} \leq 1.20$
^{4}He	2.8(−3)	2.8(−3)	2.8(−3)
^{12}C	4.6(−2)	0.0	0.0
^{16}O	0.14	2.4(−4)	4.2(−2)
^{20}Ne	2.0(−3)	0.0	0.0
^{24}Mg	8.5(−3)	0.0	2.1(−3)
^{28}Si	0.15	9.5(−2)	0.14
^{32}S	8.3(−2)	5.6(−2)	7.8(−2)
^{36}Ar	1.5(−2)	1.1(−2)	1.4(−2)
^{40}Ca	1.2(−2)	1.0(−2)	1.2(−2)
^{44}Ti	0.0	0.0	0.0
^{48}Cr	2.1(−4)	2.1(−4)	2.1(−4)
^{52}Fe	4.1(−3)	4.1(−3)	4.1(−3)
^{56}Ni	0.59	0.59	0.59
^{14}N	0.0	0.0	0.0
^{22}Ne	2.4(−3)	0.0	0.0
^{56}Fe	2.7(−2)	2.7(−2)	2.7(−2)
^{54}Fe	0.11	0.10	0.11
^{58}Ni	0.13	0.13	0.13
others	6.1(−2)	5.3(−2)	5.6(−2)
sum	1.38	1.08	1.20

(unit:$M_\odot$)

Table 2.3: The detailed composition structure of the deflagration model W7. In order to compare with late detonation models W7DN or W7DT, the mass of synthesized elements inner than 1.08 $M_\odot$ and 1.20 $M_\odot$, which are corresponding to W7DN and W7DT(W7DHE), respectively, are also presented. The item 1.2(−3) means that there exist that element of $1.2\times10^{-3}M_\odot$, for example. The item less than 1.0×10^{-5} is presented by 0.0. These are same in Tables 2.4 ∼ 2.7, 5.1.

element	total	deflag.	late deto.
^{4}He	3.1(−3)	3.1(−3)	1.4(−5)
^{12}C	4.9(−5)	0.0	4.8(−5)
^{16}O	4.6(−2)	4.1(−2)	5.5(−3)
^{20}Ne	2.4(−5)	0.0	2.2(−5)
^{24}Mg	1.6(−3)	1.5(−3)	1.2(−4)
^{28}Si	0.20	0.14	5.9(−2)
^{32}S	0.12	7.8(−2)	3.9(−2)
^{36}Ar	2.3(−2)	1.4(−2)	8.8(−3)
^{40}Ca	2.1(−2)	1.2(−2)	8.7(−3)
^{44}Ti	0.0	0.0	0.0
^{48}Cr	4.1(−4)	2.0(−4)	2.1(−4)
^{52}Fe	6.8(−3)	4.1(−3)	2.8(−3)
^{56}Ni	0.63	0.59	4.0(−2)
^{14}N	0.0	0.0	0.0
^{22}Ne	0.0	0.0	0.0
^{56}Fe	2.6(−2)	2.6(−2)	0.0
^{54}Fe	0.11	0.10	8.2(−2)
^{58}Ni	0.13	0.13	7.5(−4)
others	6.7(−2)	6.5(−2)	2.8(−3)
sum	1.38	1.20	0.18

(unit:$M_{\odot}$)

Table 2.4: The detailed composition structure of the late detonation model W7DN. The elements produced in deflagration region and late detonation region, i.e., inner than or outer than the transition point where the deflagration wave from center transforms to detonation wave, are presented separately.

element	total	deflag.	late deto.
^{4}He	3.0(−3)	2.7(−3)	3.1(−4)
^{12}C	4.1(−5)	0.0	4.0(−5)
^{16}O	3.6(−3)	0.0	3.6(−3)
^{20}Ne	1.6(−5)	0.0	1.6(−5)
^{24}Mg	5.2(−5)	0.0	5.1(−5)
^{28}Si	0.14	9.5(−2)	4.4(−2)
^{32}S	8.5(−2)	5.6(−2)	2.9(−2)
^{36}Ar	1.7(−2)	1.1(−2)	6.6(−3)
^{40}Ca	1.7(−2)	1.0(−2)	7.3(−3)
^{44}Ti	1.3(−5)	0.0	0.0
^{48}Cr	4.6(−4)	2.0(−4)	2.6(−4)
^{52}Fe	9.2(−3)	4.1(−3)	5.2(−3)
^{56}Ni	0.77	0.59	0.18
^{14}N	0.0	0.0	0.0
^{22}Ne	0.0	0.0	0.0
^{56}Fe	2.7(−2)	2.7(−2)	1.9(−5)
^{54}Fe	0.11	0.10	1.1(−2)
^{58}Ni	0.13	0.13	4.1(−3)
others	6.0(−2)	5.3(−2)	6.8(−3)
sum	1.38	1.08	0.30

(unit:$M_{\odot}$)

Table 2.5: Same as Table 2.4 but for W7DT.

element	total	deflag.	late deto.
^{4}He	4.1(−3)	2.9(−3)	1.2(−3)
^{12}C	1.4(−5)	0.0	1.3(−5)
^{16}O	7.8(−4)	0.0	7.7(−4)
^{20}Ne	0.0	0.0	0.0
^{24}Mg	1.1(−5)	0.0	0.0
^{28}Si	0.13	0.12	9.2(−3)
^{32}S	8.0(−2)	7.4(−2)	6.8(−3)
^{36}Ar	1.6(−2)	1.5(−2)	1.8(−3)
^{40}Ca	1.6(−2)	1.4(−2)	2.1(−3)
^{44}Ti	1.4(−5)	1.0(−5)	0.0
^{48}Cr	3.6(−4)	2.8(−4)	8.5(−5)
^{52}Fe	6.8(−3)	5.2(−3)	1.6(−3)
^{56}Ni	0.77	0.68	8.7(−2)
^{14}N	0.0	0.0	0.0
^{22}Ne	0.0	0.0	0.0
^{56}Fe	3.1(−2)	3.1(−2)	0.0
^{54}Fe	0.12	0.12	2.8(−3)
^{58}Ni	0.14	0.14	2.9(−3)
others	6.5(−2)	6.1(−2)	4.7(−3)
sum	1.38	1.26	0.12

(unit:$M_{\odot}$)

Table 2.6: Same as Table 2.4 but for W8DT.

element	total	deflag.	late deto.
^{4}He	3.2(−2)	3.4(−3)	2.9(−2)
^{12}C	0.0	0.0	0.0
^{16}O	3.9(−3)	3.9(−3)	0.0
^{20}Ne	0.0	0.0	0.0
^{24}Mg	1.3(−5)	1.0(−5)	0.0
^{28}Si	0.16	0.16	1.2(−5)
^{32}S	8.8(−2)	8.8(−2)	3.1(−5)
^{36}Ar	1.6(−2)	1.6(−2)	6.1(−5)
^{40}Ca	1.4(−2)	1.4(−2)	9.4(−5)
^{44}Ti	1.9(−4)	1.4(−5)	1.7(−4)
^{48}Cr	3.8(−4)	2.1(−4)	1.7(−4)
^{52}Fe	4.6(−3)	4.2(−3)	4.7(−4)
^{56}Ni	0.73	0.59	0.13
^{14}N	0.0	0.0	0.0
^{22}Ne	0.0	0.0	0.0
^{56}Fe	2.7(−2)	2.7(−2)	0.0
^{54}Fe	0.11	0.11	0.0
^{58}Ni	0.13	0.13	8.5(−5)
others	7.0(−2)	5.6(−2)	1.4(−2)
sum	1.38	1.20	0.18

(unit:$M_{\odot}$)

Table 2.7: Same as Table 2.4 but for W7DHE.

element	W7	CO2.9	CO2.9B	CO2.1	CO1.8
^{4}He	8.8(−5)	2.9(−2)	4.0(−2)	3.0(−2)	6.6(−2)
^{12}C	4.7(−2)	0.11	0.11	4.3(−2)	4.6(−2)
^{16}O	0.12	0.79	0.75	0.41	0.17
^{20}Ne	2.1(−3)	0.19	0.18	3.4(−2)	5.1(−2)
^{24}Mg	3.0(−2)	7.0(−2)	7.1(−2)	5.5(−2)	3.3(−2)
^{28}Si	0.19	9.1(−2)	7.7(−2)	6.8(−2)	3.8(−3)
^{32}S	0.10	6.4(−2)	5.6(−2)	3.1(−2)	4.2(−4)
^{36}Ar	2.4(−2)	1.5(−2)	1.4(−2)	7.2(−3)	1.4(−4)
^{40}Ca	3.5(−2)	1.8(−2)	1.5(−2)	8.0(−3)	2.0(−4)
^{44}Ti	4.6(−5)	1.1(−4)	2.1(−4)	2.0(−4)	9.5(−4)
^{48}Cr	8.1(−4)	2.4(−4)	2.5(−4)	1.9(−4)	6.9(−4)
^{52}Fe	3.1(−3)	3.0(−3)	2.3(−3)	1.2(−3)	1.5(−3)
^{56}Ni	0.82	0.12	0.20	0.13	0.23
sum	1.38	1.50	1.50	0.82	0.60
$E_{\rm kin}/10^{51}$erg	1.20	1.00	1.40	1.00	1.00

(unit:$M_{\odot}$)

Table A.1: The amount of synthesized elements in the explosion of stripped C+O star models CO2.9, CO2.1, and CO1.8 whose mass is 2.9, 2.1, 1.8 $M_{\odot}$, respectively. They produce neutron stars of mass of 1.4, 1.28, 1.2 $M_{\odot}$, respectively. CO2.9B has the same initial model and mass cut as CO2.9 but its total kinematic energy is 1.4 $\times 10^{51}$ erg. Those of white dwarf deflagration model W7 are also listed for comparison.

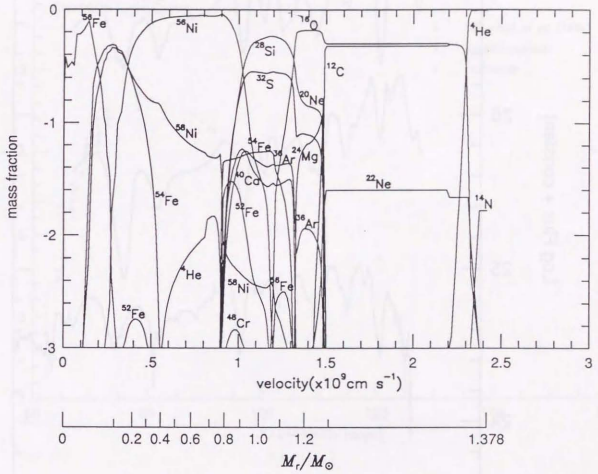

Figure 1.1: Composition of the deflagration model W7 as a function of the expansion velocity and $M_{\rm r}$ (NTY [59]). Detailed nucleosynthesis is performed by new code.

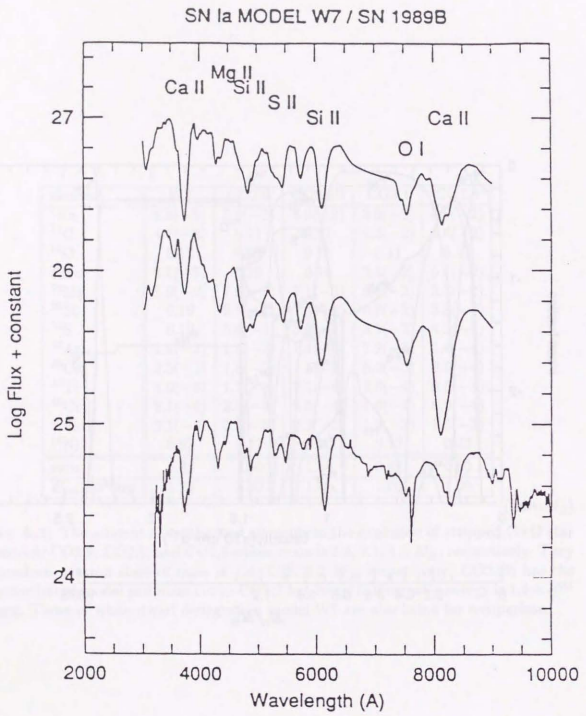

Figure 1.2: The maximum light spectrum of SN 1989B is compared with a synthetic spectrum for the carbon deflagration model W7 with no mixing (top) and mixing for $v > 11{,}000$ km s^{-1} (middle) (Harkness 1991a [23]).

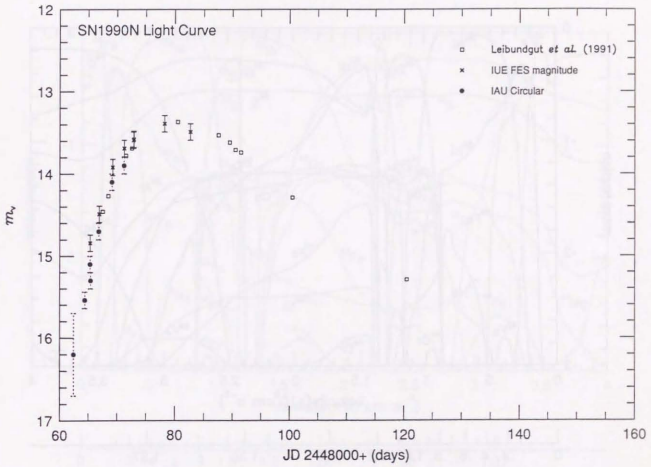

Figure 1.3: Observed visual light curve of SN 1990N.

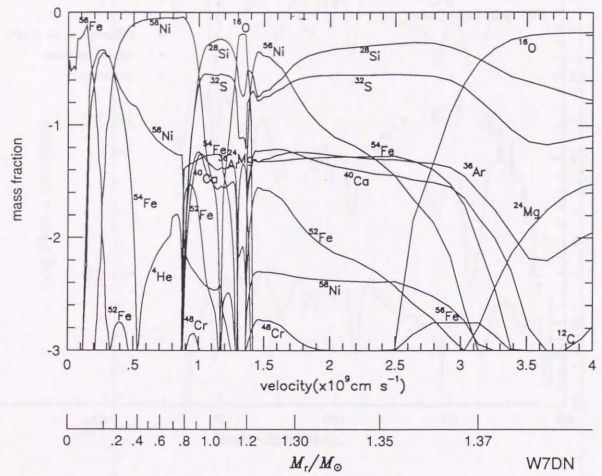

Figure 2.1: Composition of the late detonation model W7DN as a function of the expansion velocity and M_r, where the transition from deflagration to detonation takes place at $M_r = 1.20\ M_\odot$.

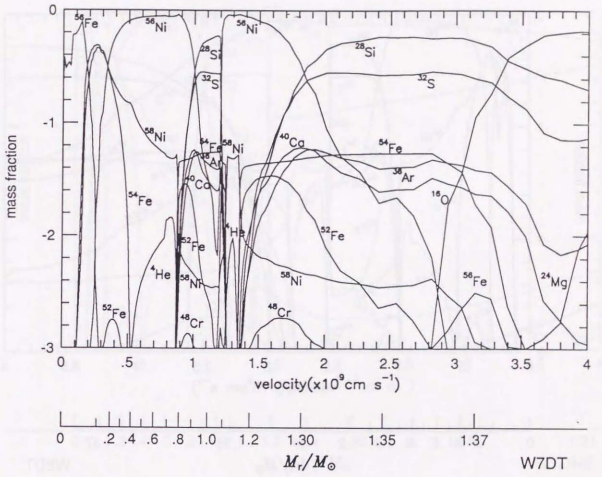

Figure 2.2: Same as Figure 2.1 but for W7DT with the transition at $M_r = 1.13$ $M_\odot$.

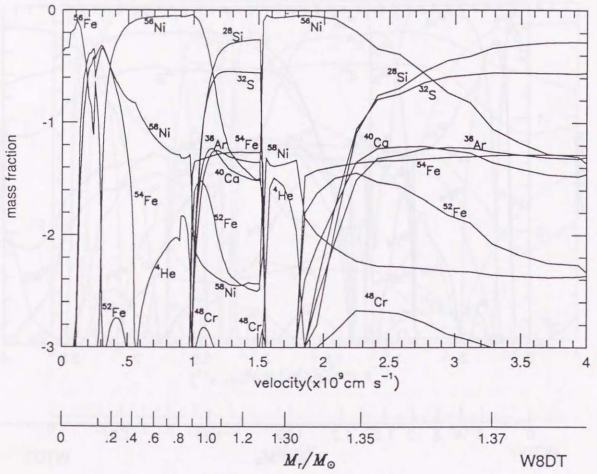

Figure 2.3: Same as Figure 2.1 but for W8DT which is based on the deflagration model W8 with the transition at $M_r = 1.25\ M_\odot$.

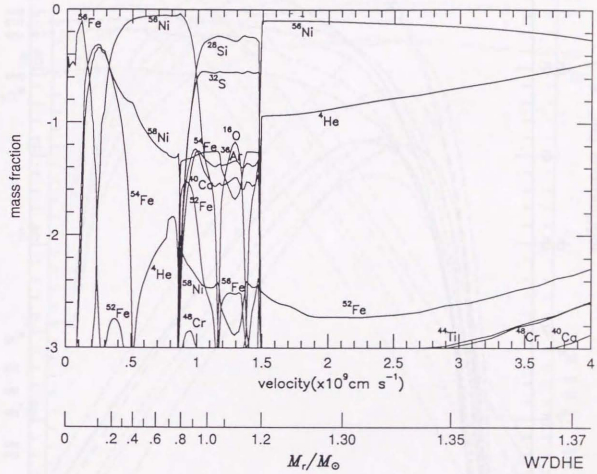

Figure 2.4: Same as Figure 2.1 but for W7DHE with the transition at $M_r = 1.20\ M_\odot$. In the initial model, C+O at $M_r \geq 1.20\ M_\odot$ has been artificially replaced with helium.

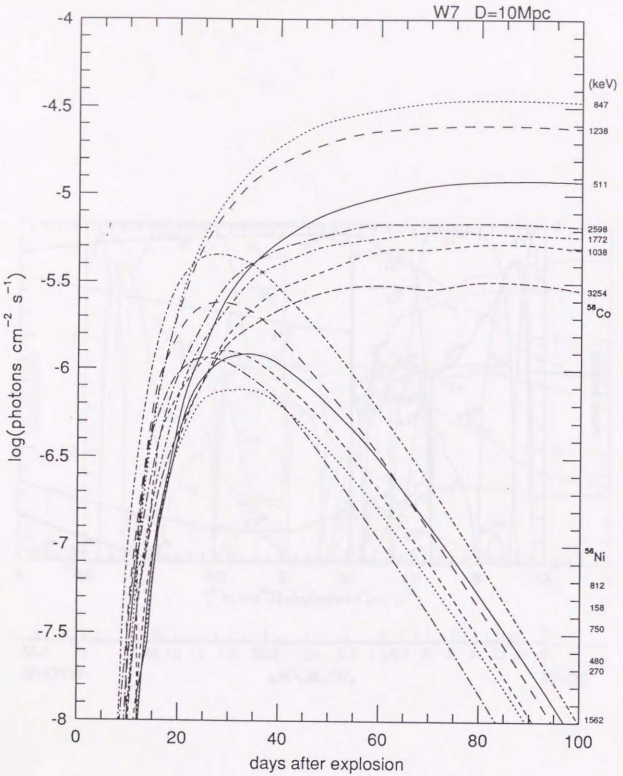

Figure 2.5: Light curves of dominant γ-ray lines from the ^{56}Ni the ^{56}Co decay for model W7 at a distance of 10 Mpc (Kumagai *et al.* 1992 [38]).

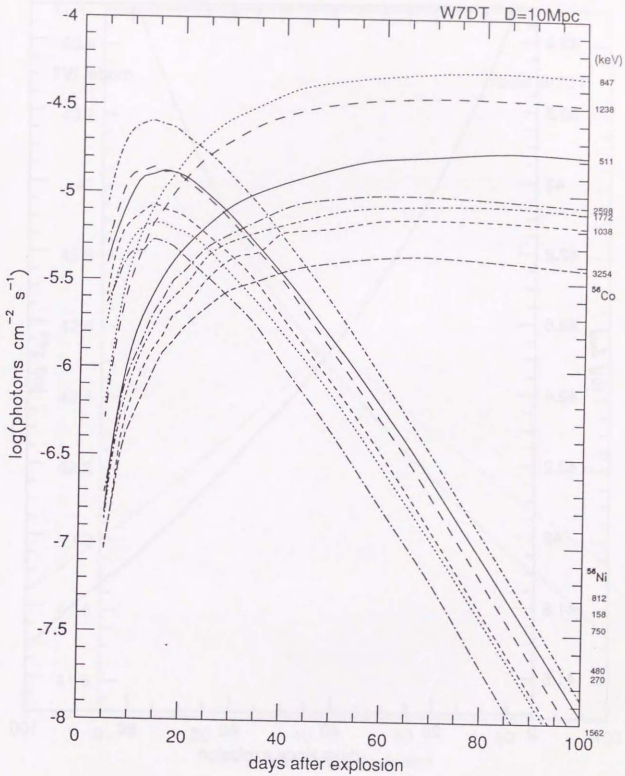

Figure 2.6: Same as Figure 6.1 but for W7DT (Kumagai *et al.* 1992 [38]).

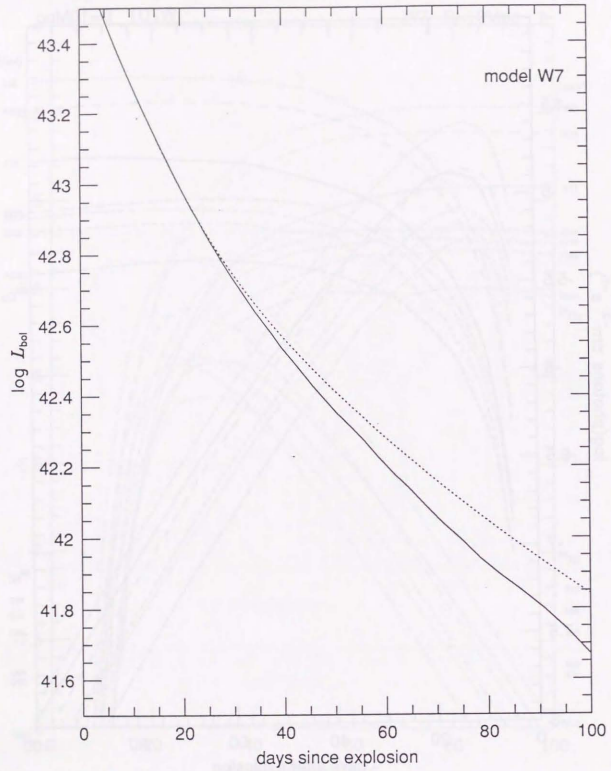

Figure 3.1: Calculated deposition functions based on W7 model. The solid line reveals the results using Monte Carlo simulation of X-ray transfer. The dotted line is the results obtained with constant κ_γ.

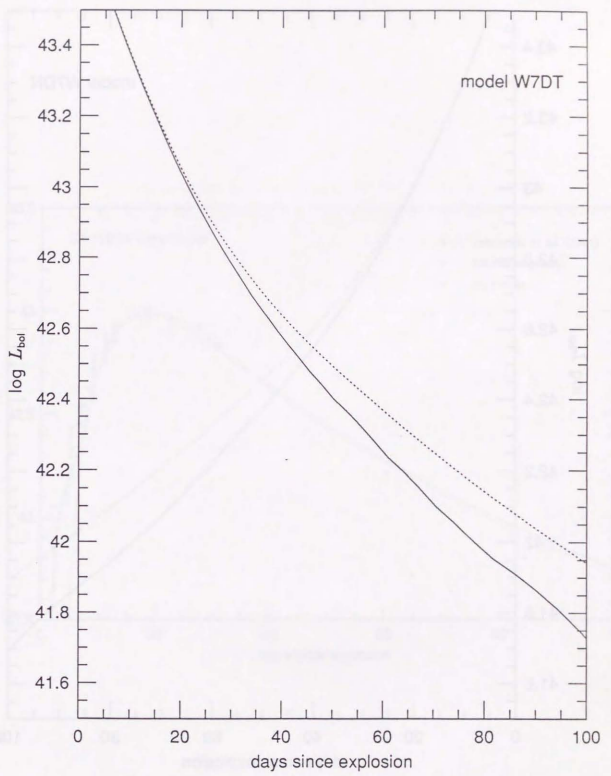

Figure 3.2: Same as Figure 3.1 but for W7DT model. The differences from Figure 3.1 in the early evolution are due to ^{56}Ni synthesized by late detonation wave in outer region.

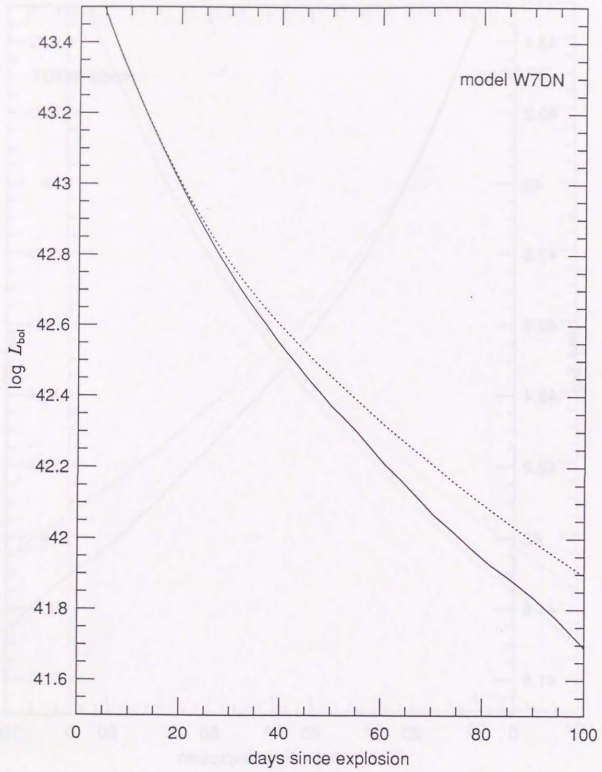

Figure 3.3: Same as Figure 3.1 but for W7DN model.

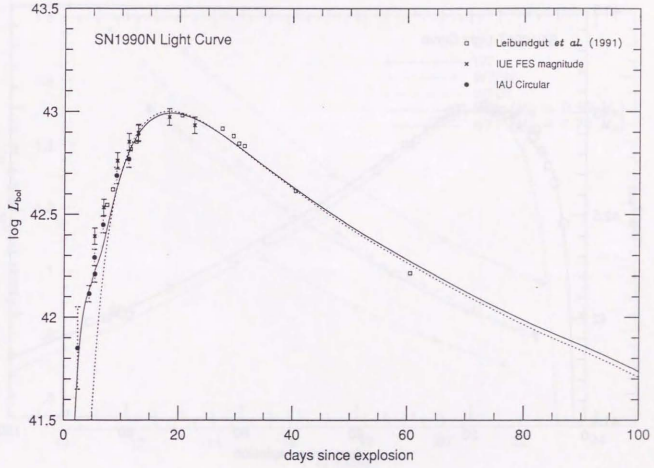

Figure 3.4: Bolometric light curve of W7DN. The optical opacity κ_{opt} is set on 0.3 $cm^2\ g^{-1}$. The light curve of W7 with the same optical opacity is also presented for comparison by dotted line. Observation of visual magnitude of SN 1990N is plotted with arbitrary shift.

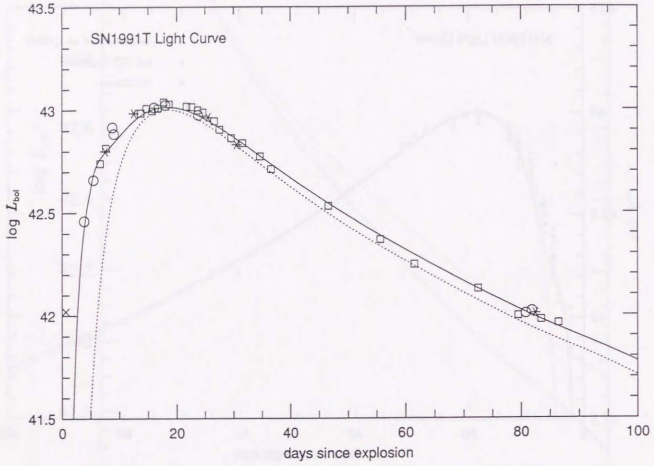

Figure 3.5: Same as Figure 3.4 but for W7DT. The observed visual magnitude of SN 1991T is also plotted with arbitrary shift.

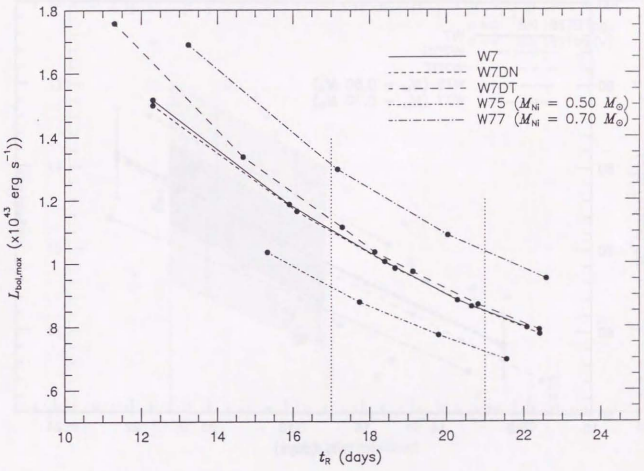

Figure 4.1: The theoretical maximum luminosities $L_{\rm max,th}$ as a function of rise time $t_{\rm R}$. $L_{\rm max,th}$ of W7, W7DN, W7DT, W75, W77 (see text) are shown.

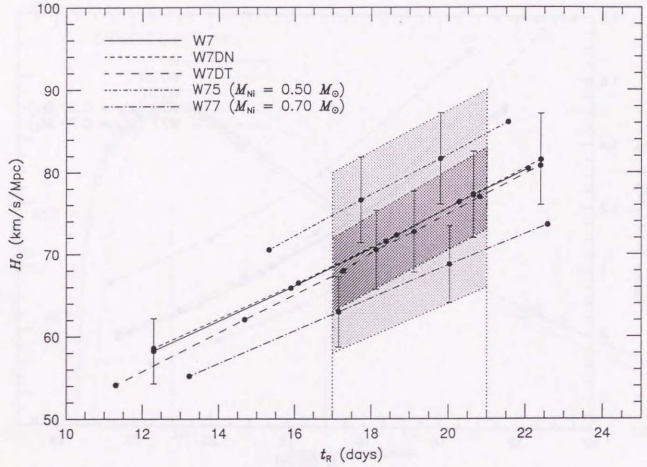

Figure 4.2: The Hubble constant H_0 with the models W7, W7DN, W7DT, W75, W77 a function of rise time t_R. Error bars are the reflections of the error term in Equation 4.2.

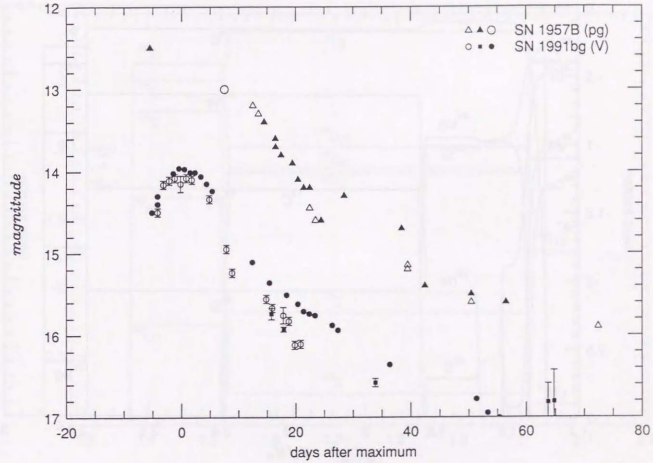

Figure A.1: Observed light curve of peculiar type Ia supernova 1991bg (Kikuchi *et al.* 1992 [34], Leibundgut *et al.* 1992 [42]). The light curve of type Ia supernova 1957B appeared in the same galaxy is also shown (LTCC91 [41]).

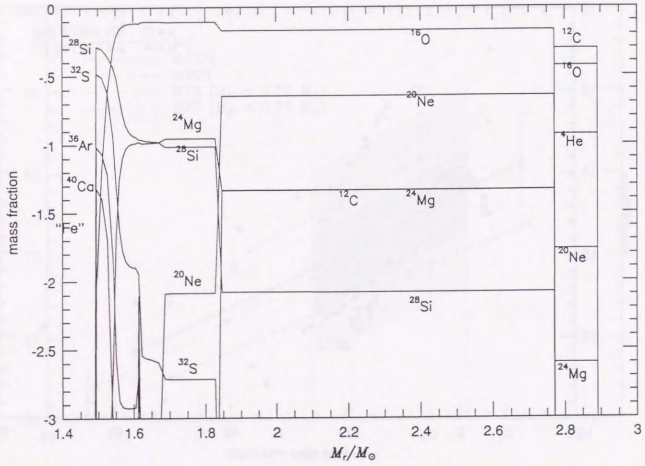

Figure A.2: The composition structure of the stripped C+O star whose mass is 2.9 $M_\odot$. This model corresponds to the massive star whose main-sequence mass is 18 $M_\odot$ and to 5 $M_\odot$ helium star.

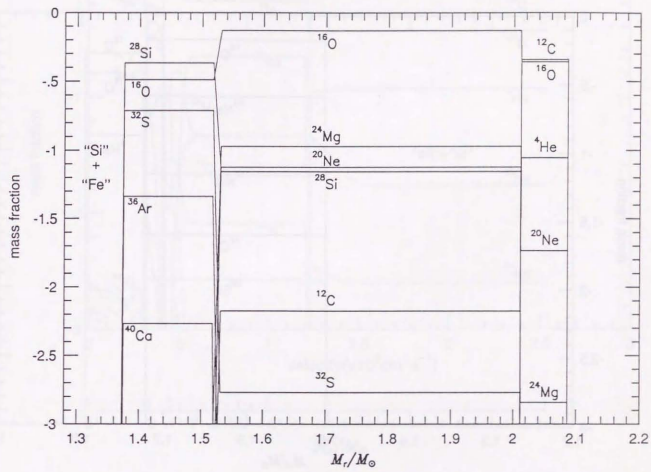

Figure A.3: Same as Figure A.2 but for 2.1 $M_\odot$ C+O star. This model corresponds to the massive star whose main-sequence mass is 15 $M_\odot$ and to the helium star whose mass is 4.0 $M_\odot$.

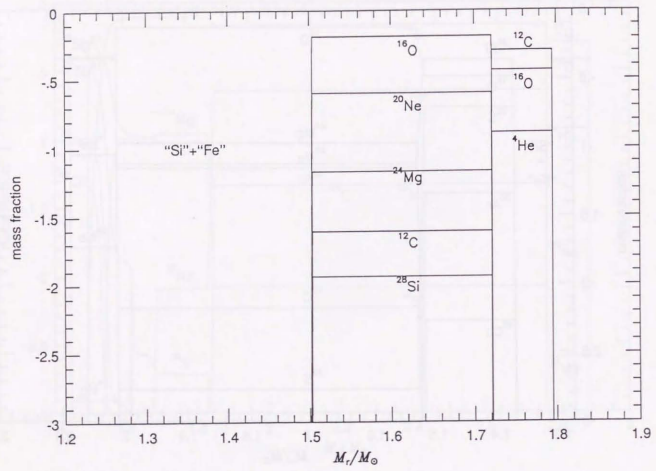

Figure A.4: Same as Figure A.2 but for 1.8 $M_\odot$ C+O star. This model corresponds to the massive star whose main-sequence mass is 13 $M_\odot$ and to the helium star whose mass is 3.3 $M_\odot$.

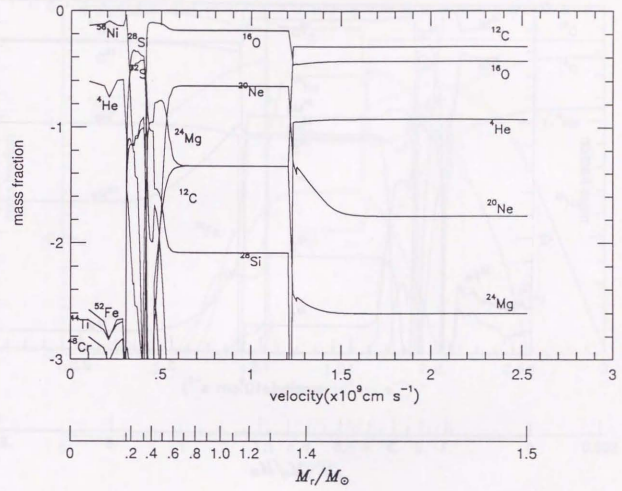

Figure A.5: Composition of the stripped C+O star explosion model CO2.9 as a function of the expansion velocity and M_r. The point of mass cut is set to 1.4 $M_\odot$, where $M_r = 0$ in this figure. Total kinematic energy of ejecta is 1.0×10^{51} erg.

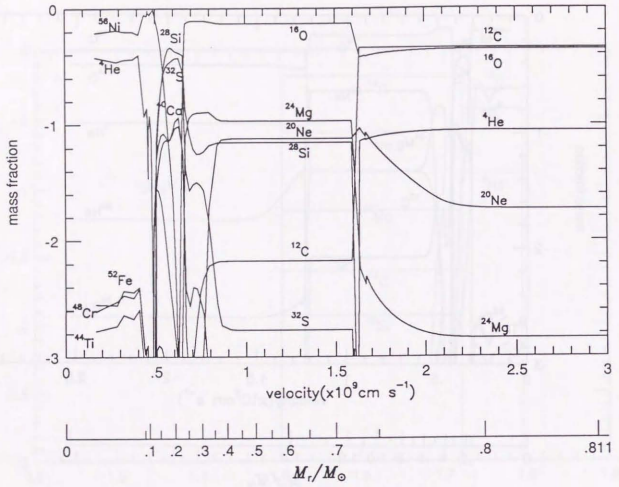

Figure A.6: Same as Figure A.5 but for CO2.1. The point of mass cut is set to 1.28 $M_\odot$, where $M_r = 0$ in this figure. Total kinematic energy of ejecta is 1.0 $\times$ 10^{51} erg.

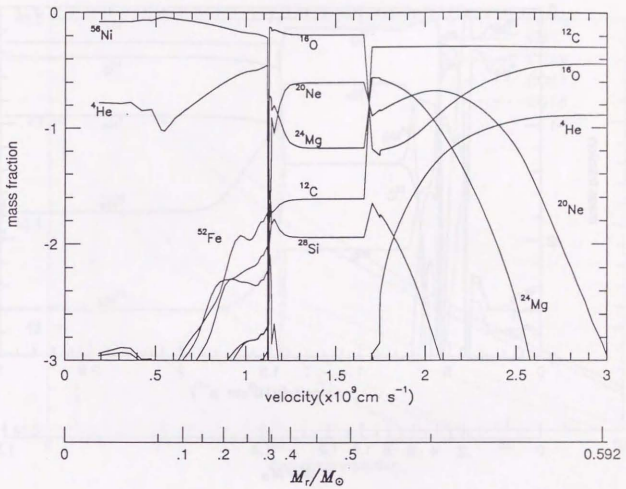

Figure A.7: Same as Figure A.5 but for CO1.8. The point of mass cut is set to 1.2 $M_\odot$, where $M_r = 0$ in this figure. Total kinematic energy of ejecta is 1.0 $\times$ 10^{51} erg.

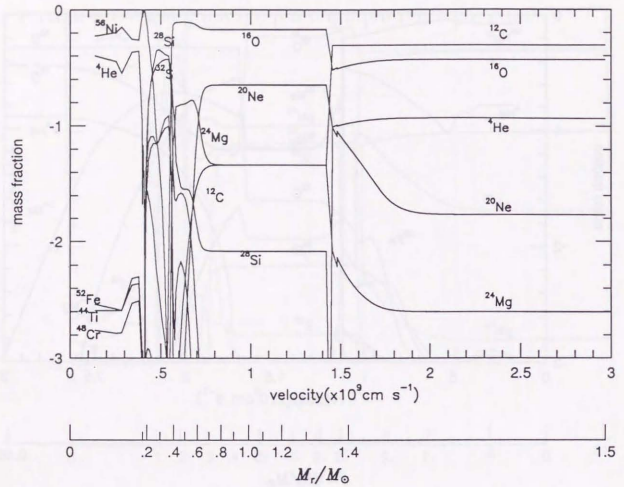

Figure A.8: Same as Figure A.5 but for CO2.9B. Total kinematic energy of ejecta is 1.4×10^{51} erg. Because of the larger energy at the mass cut point than CO2.9, a larger amount of ^{56}Ni is synthesized.

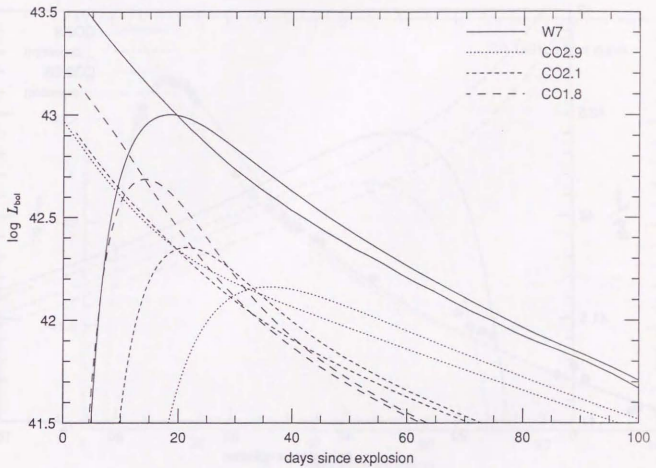

Figure A.9: Theoretical light curves and deposition functions with the stripped C+O star explosion models. For comparison, those of white dwarf deflagration model W7 are also presented.

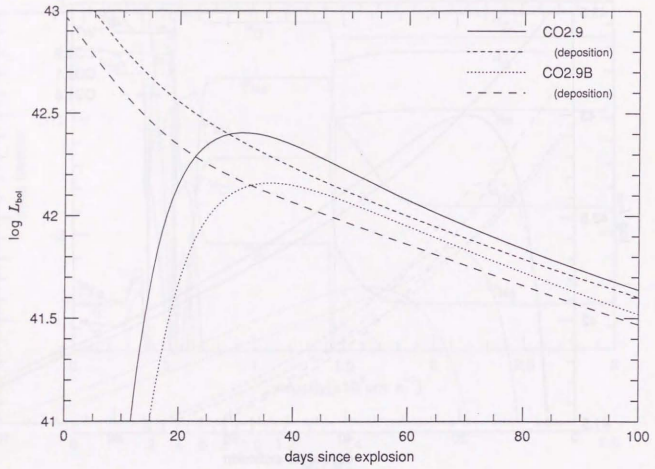

Figure A.10: Same as Figure A.9 but for CO2.9B. The light curve and deposition function for CO2.9 are also plotted for comparison.

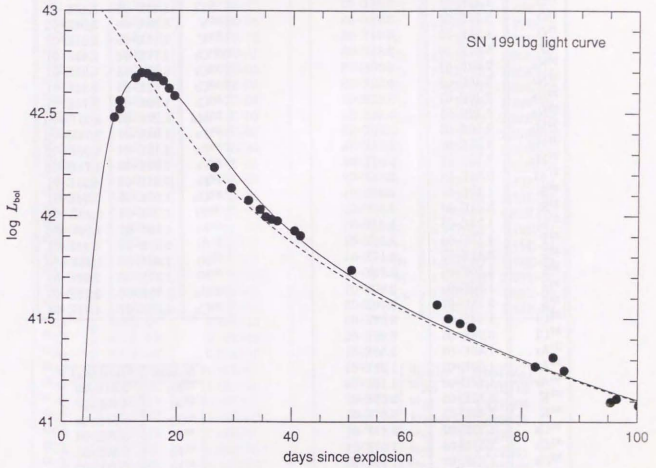

Figure A.11: Bolometric light curve for CO1.8 with observations of visual magnitude of SN 1991bg is plotted with arbitrary shift (Leibundgut *et al.* 1992 [42]).

Species	Mass($M_\odot$)	$< X_i/X_i(^{56}\mathrm{Fe}) >$
^{12}C	4.83E−02	2.73E−02
^{13}C	1.40E−06	6.59E−05
^{14}N	1.16E−06	2.70E−06
^{15}N	1.32E−09	7.82E−07
^{16}O	1.43E−01	3.66E−02
^{17}O	3.54E−08	2.28E−05
^{18}O	8.25E−10	9.21E−08
^{19}F	5.67E−10	2.88E−06
^{20}Ne	2.02E−03	3.30E−03
^{21}Ne	8.46E−06	4.33E−03
^{22}Ne	2.49E−03	3.02E−02
^{23}Na	6.32E−05	3.45E−03
^{24}Mg	8.50E−03	3.20E−02
^{25}Mg	4.05E−05	1.14E−03
^{26}Mg	3.18E−05	7.81E−04
^{27}Al	9.86E−04	3.24E−02
^{28}Si	1.50E−01	4.38E−01
^{29}Si	8.61E−04	4.76E−02
^{30}Si	1.74E−03	1.41E−01
^{31}P	4.18E−04	1.56E−01
^{32}S	8.41E−02	4.17E−01
^{33}S	4.50E−04	2.70E−01
^{34}S	1.90E−03	2.00E−01
^{36}S	3.15E−07	9.70E−03
^{35}Cl	1.34E−04	8.07E−02
^{37}Cl	3.98E−05	6.98E−02
^{36}Ar	1.49E−02	3.50E−01
^{38}Ar	1.06E−03	1.25E−01
^{40}Ar	1.26E−08	1.19E−04
^{39}K	8.52E−05	5.05E−02
^{41}K	7.44E−06	5.67E−02
^{40}Ca	1.23E−02	3.81E−01
^{42}Ca	3.51E−05	1.57E−01
^{43}Ca	1.03E−07	1.99E−03
^{44}Ca	8.86E−06	1.18E−02
^{46}Ca	1.99E−09	1.58E−03
^{48}Ca	7.10E−12	9.61E−08
^{45}Sc	2.47E−07	1.34E−02
^{46}Ti	1.71E−05	1.47E−01
^{47}Ti	6.04E−07	5.53E−03
^{48}Ti	2.03E−04	1.79E−01
^{49}Ti	1.69E−05	1.96E−01
^{50}Ti	1.26E−05	1.48E−01
^{50}V	8.28E−09	2.04E−02
^{51}V	5.15E−05	3.01E−01
^{50}Cr	2.71E−04	7.45E−01
^{52}Cr	5.15E−03	7.03E−01
^{53}Cr	7.85E−04	9.23E−01
^{54}Cr	1.89E−04	8.75E−01
^{55}Mn	8.23E−03	1.21E+00
^{54}Fe	1.04E−01	2.78E+00
^{56}Fe	6.13E−01	1.00E+00
^{57}Fe	2.55E−02	1.71E+00
^{58}Fe	9.63E−04	4.21E−01
^{59}Co	1.02E−03	5.94E−01
^{58}Ni	1.28E−01	5.13E+00
^{60}Ni	1.05E−02	1.06E+00
^{61}Ni	2.51E−04	5.44E−01
^{62}Ni	2.66E−03	1.85E+00
^{64}Ni	1.31E−06	2.99E−03
^{63}Cu	1.79E−06	5.73E−03
^{65}Cu	6.83E−07	4.74E−03

Species	Mass($M_\odot$)
^{22}Na	2.81E−08
^{26}Al	4.70E−07
^{44}Ti	8.81E−06
^{48}V	5.90E−08
^{56}Ni	5.89E−01
^{57}Ni	2.41E−02
^{56}Co	1.67E−04
^{57}Co	1.32E−03
^{60}Co	1.62E−07
^{60}Fe	2.49E−08

Table C.1: (Left and upper right) Nucleosynthesis products for the deflagration model W7 after the radioactive decay. $< X_i/X_i(^{56}\mathrm{Fe}) > \equiv [X_i/X_i(^{56}\mathrm{Fe})]/[X_i/X_i(^{56}\mathrm{Fe})]_\odot$. (Below right) γ-radioactivities from W7.

Species	Mass($M_\odot$)	$< X_i/X_i(^{56}\mathrm{Fe}) >$
^{12}C	5.79E−05	3.08E−05
^{13}C	1.36E−10	6.01E−09
^{14}N	6.29E−10	1.38E−09
^{15}N	3.86E−11	2.15E−08
^{16}O	4.71E−02	1.13E−02
^{17}O	1.09E−10	6.61E−08
^{18}O	7.05E−12	7.41E−10
^{19}F	2.09E−12	1.00E−08
^{20}Ne	2.86E−05	4.39E−05
^{21}Ne	1.67E−08	8.05E−06
^{22}Ne	1.33E−09	1.52E−08
^{23}Na	4.69E−07	2.41E−05
^{24}Mg	1.64E−03	5.81E−03
^{25}Mg	7.99E−07	2.12E−05
^{26}Mg	2.01E−06	4.64E−05
^{27}Al	9.56E−05	2.95E−03
^{28}Si	2.02E−01	5.56E−01
^{29}Si	2.19E−04	1.14E−02
^{30}Si	3.67E−04	2.81E−02
^{31}P	1.40E−04	4.92E−02
^{32}S	1.19E−01	5.57E−01
^{33}S	1.97E−04	1.11E−01
^{34}S	2.01E−03	1.99E−01
^{36}S	4.71E−08	1.36E−03
^{35}Cl	8.38E−05	4.74E−02
^{37}Cl	3.14E−05	5.18E−02
^{36}Ar	2.31E−02	5.09E−01
^{38}Ar	1.26E−03	1.40E−01
^{40}Ar	2.92E−09	2.59E−05
^{39}K	9.60E−05	5.36E−02
^{41}K	7.65E−06	5.49E−02
^{40}Ca	2.10E−02	6.15E−01
^{42}Ca	4.07E−05	1.72E−01
^{43}Ca	4.97E−08	9.00E−04
^{44}Ca	1.01E−05	1.26E−02
^{46}Ca	2.88E−10	2.15E−04
^{48}Ca	9.81E−12	1.25E−07
^{45}Sc	3.02E−07	1.54E−02
^{46}Ti	1.94E−05	1.57E−01
^{47}Ti	5.84E−07	5.03E−03
^{48}Ti	4.03E−04	3.35E−01
^{49}Ti	3.59E−05	3.93E−01
^{50}Ti	1.27E−05	1.40E−01
^{50}V	2.55E−08	5.92E−02
^{51}V	1.16E−04	6.35E−01
^{50}Cr	4.08E−04	1.06E+00
^{52}Cr	7.94E−03	1.02E+00
^{53}Cr	1.45E−03	1.60E+00
^{54}Cr	1.93E−04	8.39E−01
^{55}Mn	1.82E−02	2.52E+00
^{54}Fe	1.07E−01	2.69E+00
^{56}Fe	6.51E−01	1.00E+00
^{57}Fe	2.90E−02	1.83E+00
^{58}Fe	9.37E−04	3.86E−01
^{59}Co	1.79E−03	9.78E−01
^{58}Ni	1.28E−01	4.83E+00
^{60}Ni	6.55E−03	6.19E−01
^{61}Ni	1.05E−04	2.15E−01
^{62}Ni	1.34E−03	8.78E−01
^{64}Ni	1.86E−06	3.99E−03
^{63}Cu	5.56E−06	1.68E−02
^{65}Cu	1.89E−07	1.24E−03

Species	Mass($M_\odot$)
^{22}Na	7.57E−10
^{26}Al	1.47E−08
^{44}Ti	1.01E−05
^{48}V	5.52E−08
^{56}Ni	6.27E−01
^{57}Ni	2.60E−02
^{56}Co	4.97E−04
^{57}Co	2.75E−03
^{60}Co	6.40E−07
^{60}Fe	7.55E−08

Table C.2: Same as Table C.1 but for the late detonation model W7DN.

Species	Mass($M_\odot$)	$< X_i/X_i(^{56}\mathrm{Fe}) >$
^{12}C	4.80E−05	2.10E−05
^{13}C	8.98E−11	3.28E−09
^{14}N	2.96E−10	5.34E−10
^{15}N	3.05E−11	1.40E−08
^{16}O	4.09E−03	8.12E−04
^{17}O	6.32E−11	3.14E−08
^{18}O	6.01E−12	5.20E−10
^{19}F	1.79E−12	7.04E−09
^{20}Ne	2.01E−05	2.54E−05
^{21}Ne	1.14E−08	4.53E−06
^{22}Ne	8.59E−10	8.08E−09
^{23}Na	3.48E−07	1.47E−05
^{24}Mg	6.33E−05	1.85E−04
^{25}Mg	2.72E−07	5.93E−06
^{26}Mg	8.58E−07	1.63E−05
^{27}Al	6.25E−06	1.59E−04
^{28}Si	1.43E−01	3.23E−01
^{29}Si	1.96E−05	8.38E−04
^{30}Si	2.24E−05	1.41E−03
^{31}P	1.34E−05	3.88E−03
^{32}S	8.62E−02	3.31E−01
^{33}S	2.57E−05	1.20E−02
^{34}S	1.55E−04	1.26E−02
^{36}S	7.30E−09	1.74E−04
^{35}Cl	1.13E−05	5.28E−03
^{37}Cl	5.47E−06	7.44E−03
^{36}Ar	1.75E−02	3.17E−01
^{38}Ar	1.19E−04	1.09E−02
^{40}Ar	7.19E−10	5.25E−06
^{39}K	1.22E−05	5.61E−03
^{41}K	1.41E−06	8.33E−03
^{40}Ca	1.75E−02	4.20E−01
^{42}Ca	4.02E−06	1.40E−02
^{43}Ca	5.56E−08	8.29E−04
^{44}Ca	1.34E−05	1.38E−02
^{46}Ca	1.29E−10	7.93E−05
^{48}Ca	8.70E−12	9.12E−08
^{45}Sc	1.48E−07	6.20E−03
^{46}Ti	2.86E−06	1.91E−02
^{47}Ti	5.26E−07	3.73E−03
^{48}Ti	4.54E−04	3.11E−01
^{49}Ti	3.64E−05	3.28E−01
^{50}Ti	1.30E−05	1.19E−01
^{50}V	6.24E−09	1.19E−02
^{51}V	8.68E−05	3.93E−01
^{50}Cr	3.37E−04	7.20E−01
^{52}Cr	1.02E−02	1.08E+00
^{53}Cr	1.28E−03	1.16E+00
^{54}Cr	1.93E−04	6.91E−01
^{55}Mn	1.02E−02	1.17E+00
^{54}Fe	1.14E−01	2.36E+00
^{56}Fe	7.91E−01	1.00E+00
^{57}Fe	2.87E−02	1.49E+00
^{58}Fe	9.73E−04	3.30E−01
^{59}Co	1.07E−03	4.81E−01
^{58}Ni	1.32E−01	4.10E+00
^{60}Ni	1.12E−02	8.69E−01
^{61}Ni	2.80E−04	4.70E−01
^{62}Ni	2.95E−03	1.59E+00
^{64}Ni	1.36E−06	2.40E−03
^{63}Cu	1.98E−06	4.90E−03
^{65}Cu	7.81E−07	4.20E−03

Species	Mass($M_\odot$)
^{22}Na	5.26E−10
^{26}Al	6.24E−09
^{44}Ti	1.34E−05
^{48}V	2.73E−08
^{56}Ni	7.67E−01
^{57}Ni	2.72E−02
^{56}Co	1.76E−04
^{57}Co	1.33E−03
^{60}Co	1.63E−07
^{60}Fe	2.58E−08

Table C.3: Same as Table C.1 but for W7DT.

Species	Mass($M_o dot$)	$< X_i/X_i(^{56}Fe) >$
^{12}C	1.60E−05	6.98E−06
^{13}C	2.12E−11	7.71E−10
^{14}N	1.92E−11	3.46E−11
^{15}N	4.18E−12	1.91E−09
^{16}O	9.22E−04	1.82E−04
^{17}O	4.19E−12	2.08E−09
^{18}O	3.77E−13	3.25E−11
^{19}F	1.96E−14	7.71E−11
^{20}Ne	4.69E−06	5.90E−06
^{21}Ne	3.97E−10	1.57E−07
^{22}Ne	1.78E−10	1.66E−09
^{23}Na	7.18E−08	3.02E−06
^{24}Mg	1.25E−05	3.63E−05
^{25}Mg	2.42E−08	5.27E−07
^{26}Mg	9.79E−08	1.86E−06
^{27}Al	1.14E−06	2.89E−05
^{28}Si	1.31E−01	2.94E−01
^{29}Si	4.93E−06	2.10E−04
^{30}Si	4.33E−06	2.72E−04
^{31}P	2.90E−06	8.37E−04
^{32}S	8.16E−02	3.12E−01
^{33}S	8.77E−06	4.07E−03
^{34}S	2.63E−05	2.13E−03
^{36}S	1.18E−09	2.79E−05
^{35}Cl	2.84E−06	1.32E−03
^{37}Cl	2.37E−06	3.21E−03
^{36}Ar	1.67E−02	3.01E−01
^{38}Ar	2.17E−05	1.99E−03
^{40}Ar	4.38E−10	3.18E−06
^{39}K	3.63E−06	1.66E−03
^{41}K	7.04E−07	4.14E−03
^{40}Ca	1.62E−02	3.88E−01
^{42}Ca	8.81E−07	3.05E−03
^{43}Ca	9.64E−08	1.43E−03
^{44}Ca	1.42E−05	1.45E−02
^{46}Ca	1.37E−10	8.43E−05
^{48}Ca	6.28E−13	6.56E−09
^{45}Sc	1.27E−07	5.29E−03
^{46}Ti	1.33E−06	8.83E−03
^{47}Ti	6.41E−07	4.53E−03
^{48}Ti	3.72E−04	2.54E−01
^{49}Ti	3.16E−05	2.84E−01
^{50}Ti	3.54E−06	3.21E−02
^{50}V	4.37E−09	8.33E−03
^{51}V	7.52E−05	3.39E−01
^{50}Cr	3.07E−04	6.52E−01
^{52}Cr	7.81E−03	8.23E−01
^{53}Cr	1.14E−03	1.04E+00
^{54}Cr	7.16E−05	2.55E−01
^{55}Mn	1.06E−02	1.21E+00
^{54}Fe	1.18E−01	2.43E+00
^{56}Fe	7.94E−01	1.00E+00
^{57}Fe	3.15E−02	1.63E+00
^{58}Fe	4.47E−04	1.51E−01
^{59}Co	1.39E−03	6.22E−01
^{58}Ni	1.43E−01	4.43E+00
^{60}Ni	1.42E−02	1.10E+00
^{61}Ni	3.45E−04	5.78E−01
^{62}Ni	3.09E−03	1.66E+00
^{64}Ni	4.39E−07	7.73E−04
^{63}Cu	2.24E−06	5.54E−03
^{65}Cu	9.77E−07	5.23E−03

Species	Mass($M_\odot$)
^{22}Na	1.65E−10
^{26}Al	1.65E−09
^{44}Ti	1.42E−05
^{48}V	2.60E−08
^{56}Ni	7.67E−01
^{57}Ni	2.96E−02
^{56}Co	1.86E−04
^{57}Co	1.87E−03
^{60}Co	8.77E−08
^{60}Fe	6.37E−09

Table C.4: Same as Table C.1 but for W8DT.

Species	Mass($M_\odot dot$)	$< X_i/X_i(^{56}Fe) >$
^{12}C	6.48E−06	2.99E−06
^{13}C	5.24E−10	2.01E−08
^{14}N	4.57E−11	8.68E−11
^{15}N	7.88E−12	3.79E−09
^{16}O	3.98E−03	8.30E−04
^{17}O	1.71E−13	8.97E−11
^{18}O	2.36E−14	2.14E−12
^{19}F	3.75E−13	1.55E−09
^{20}Ne	3.16E−06	4.20E−06
^{21}Ne	6.26E−09	2.61E−06
^{22}Ne	4.01E−09	3.96E−08
^{23}Na	2.49E−09	1.11E−07
^{24}Mg	1.33E−05	4.09E−05
^{25}Mg	1.68E−06	3.86E−05
^{26}Mg	2.04E−09	4.08E−08
^{27}Al	2.54E−07	6.78E−06
^{28}Si	1.60E−01	3.80E−01
^{29}Si	4.61E−05	2.07E−03
^{30}Si	2.72E−05	1.80E−03
^{31}P	3.67E−05	1.12E−02
^{32}S	8.89E−02	3.59E−01
^{33}S	8.40E−05	4.11E−02
^{34}S	4.81E−04	4.11E−02
^{36}S	1.33E−09	3.33E−05
^{35}Cl	4.92E−05	2.41E−02
^{37}Cl	2.19E−05	3.13E−02
^{36}Ar	1.59E−02	3.03E−01
^{38}Ar	6.48E−04	6.27E−02
^{40}Ar	8.87E−10	6.80E−06
^{39}K	7.70E−05	3.72E−02
^{41}K	5.74E−06	3.57E−02
^{40}Ca	1.37E−02	3.46E−01
^{42}Ca	2.08E−05	7.60E−02
^{43}Ca	2.72E−06	4.26E−02
^{44}Ca	1.95E−04	2.11E−01
^{46}Ca	1.22E−10	7.88E−05
^{48}Ca	8.78E−12	9.68E−08
^{45}Sc	1.34E−06	5.89E−02
^{46}Ti	8.48E−05	5.96E−01
^{47}Ti	3.31E−05	2.47E−01
^{48}Ti	3.88E−04	2.79E−01
^{49}Ti	2.32E−05	2.20E−01
^{50}Ti	1.32E−05	1.27E−01
^{50}V	6.80E−09	1.37E−02
^{51}V	1.31E−04	6.22E−01
^{50}Cr	4.36E−04	9.78E−01
^{52}Cr	5.69E−03	6.33E−01
^{53}Cr	8.10E−04	7.75E−01
^{54}Cr	1.94E−04	7.29E−01
^{55}Mn	8.41E−03	1.01E+00
^{54}Fe	1.07E−01	2.33E+00
^{56}Fe	7.53E−01	1.00E+00
^{57}Fe	2.79E−02	1.53E+00
^{58}Fe	9.72E−04	3.46E−01
^{59}Co	2.28E−03	1.08E+00
^{58}Ni	1.30E−01	4.24E+00
^{60}Ni	1.88E−02	1.54E+00
^{61}Ni	4.93E−04	8.72E−01
^{62}Ni	3.02E−03	1.71E+00
^{64}Ni	1.37E−06	2.55E−03
^{63}Cu	4.16E−05	1.08E−01
^{65}Cu	6.35E−06	3.59E−02

Species	Mass($M_\odot$)
^{22}Na	5.34E−11
^{26}Al	2.99E−09
^{44}Ti	1.95E−04
^{48}V	4.10E−08
^{56}Ni	7.28E−01
^{57}Ni	2.65E−02
^{56}Co	1.69E−04
^{57}Co	1.34E−03
^{60}Co	1.67E−07
^{60}Fe	2.68E−08

Table C.5: Same as Table C.1 but for W7DHE.

Species	Mass($M_\odot dot$)	$< X_i/X_i(^{56}Fe) >$
^{12}C	5.08E−02	2.62E−02
^{13}C	1.56E−09	6.71E−08
^{14}N	3.31E−08	7.04E−08
^{15}N	4.13E−07	2.23E−04
^{16}O	1.33E−01	3.10E−02
^{17}O	3.32E−10	1.95E−07
^{18}O	2.69E−10	2.74E−08
^{19}F	1.37E−10	6.36E−07
^{20}Ne	2.29E−03	3.40E−03
^{21}Ne	2.81E−08	1.32E−05
^{22}Ne	2.15E−08	2.38E−07
^{23}Na	1.41E−05	7.01E−04
^{24}Mg	1.58E−02	5.41E−02
^{25}Mg	1.64E−07	4.22E−06
^{26}Mg	1.87E−07	4.19E−06
^{27}Al	1.13E−04	3.39E−03
^{28}Si	1.38E−01	3.67E−01
^{29}Si	6.03E−05	3.04E−03
^{30}Si	3.09E−05	2.29E−03
^{31}P	8.51E−05	2.90E−02
^{32}S	9.19E−02	4.15E−01
^{33}S	5.83E−05	3.20E−02
^{34}S	2.84E−06	2.72E−04
^{36}S	1.09E−11	3.05E−07
^{35}Cl	8.06E−06	4.42E−03
^{37}Cl	5.36E−06	8.59E−03
^{36}Ar	1.99E−02	4.25E−01
^{38}Ar	5.93E−07	6.43E−05
^{40}Ar	1.14E−12	9.80E−09
^{39}K	1.82E−06	9.85E−04
^{41}K	5.33E−07	3.71E−03
^{40}Ca	1.95E−02	5.54E−01
^{42}Ca	1.55E−08	6.33E−05
^{43}Ca	6.81E−08	1.20E−03
^{44}Ca	1.55E−05	1.88E−02
^{46}Ca	5.88E−11	4.26E−05
^{48}Ca	5.96E−12	7.35E−08
^{45}Sc	3.92E−08	1.93E−03
^{46}Ti	7.87E−07	6.19E−03
^{47}Ti	7.49E−07	6.26E−03
^{48}Ti	3.21E−04	2.59E−01
^{49}Ti	1.64E−06	1.74E−02
^{50}Ti	1.14E−05	1.23E−01
^{50}V	5.66E−09	1.28E−02
^{51}V	2.10E−05	1.12E−01
^{50}Cr	7.61E−05	1.91E−01
^{52}Cr	6.63E−03	8.26E−01
^{53}Cr	4.65E−04	4.98E−01
^{54}Cr	1.79E−04	7.52E−01
^{55}Mn	6.27E−03	8.43E−01
^{54}Fe	8.18E−02	1.99E+00
^{56}Fe	6.72E−01	1.00E+00
^{57}Fe	1.98E−02	1.21E+00
^{58}Fe	9.34E−04	3.72E−01
^{59}Co	1.10E−03	5.83E−01
^{58}Ni	9.67E−02	3.54E+00
^{60}Ni	1.43E−02	1.31E+00
^{61}Ni	2.30E−04	4.56E−01
^{62}Ni	1.37E−03	8.66E−01
^{64}Ni	1.22E−06	2.54E−03
^{63}Cu	2.86E−06	8.37E−03
^{65}Cu	9.60E−07	6.08E−03

Species	Mass($M_\odot$)
^{22}Na	1.91E−08
^{26}Al	2.96E−08
^{44}Ti	1.55E−05
^{48}V	1.57E−08
^{56}Ni	6.46E−01
^{57}Ni	1.81E−02
^{56}Co	1.43E−04
^{57}Co	1.63E−03
^{60}Co	1.59E−07
^{60}Fe	2.24E−08

Table C.6: Same as Table C.1 but for W7 with zero metallicity (see Sec. 2.4.4).